Department of Electronics and Nanoengineering

Photonic and Electronic Characterization of Two-dimensional Transition Metal Dichalcogenides

Abde Mayeen Shafi

Aalto University

DOCTORAL THESES

Aalto University publication series
DOCTORAL THESES 221/2023

Photonic and Electronic Characterization of Two-dimensional Transition Metal Dichalcogenides

Abde Mayeen Shafi

A doctoral thesis completed for the degree of Doctor of Science (Technology) to be defended, with the permission of the Aalto University School of Electrical Engineering, at a public examination held at the lecture hall L1 Bioproduct Centre of the school on 19 December 2023 at 12:00.

Aalto University
School of Electrical Engineering
Department of Electronics and Nanoengineering
Nanoscience and Advanced Materials

Supervising professor
Professor Harri Lipsanen, Aalto University, Finland.

Thesis advisor
Dr. David Mackenzie, Kyocera Tikitin Oy, Finland.

Preliminary examiners
Professor Sanshui Xiao, Danmarks Tekniske Universitet (DTU), Denmark.
Professor Tapio Fabritius, University of Oulu, Finland.

Opponent
Professor Polina Kuzhir, University of Eastern Finland, Finland.

Aalto University publication series
DOCTORAL THESES 221/2023

© 2023 Abde Mayeen Shafi

ISBN 978-952-64-1589-5 (printed)
ISBN 978-952-64-1590-1 (pdf)
ISSN 1799-4934 (printed)
ISSN 1799-4942 (pdf)
http://urn.fi/URN:ISBN:978-952-64-1590-1

Unigrafia Oy
Helsinki 2023

Finland

A"
Aalto University

Abstract

Aalto University, P.O. Box 11000, FI-00076 Aalto www.aalto.fi

Author
Abde Mayeen Shafi

Name of the doctoral thesis
Photonic and Electronic Characterization of Two-dimensional Transition Metal Dichalcogenides

Publisher School of Electrical Engineering

Unit Department of Electronics and Nanoengineering

Series Aalto University publication series DOCTORAL THESES 221/2023

Field of research Micro- and nanoscience

Manuscript submitted 22 September 2023 **Date of the defence** 19 December 2023

Permission for public defence granted (date) 17 November 2023 **Language** English

☐ **Monograph** ☒ **Article thesis** ☐ **Essay thesis**

Abstract
Two-dimensional (2D) transition metal dichalcogenides (TMDCs) hold promise for numerous unprecedented applications in nanophotonics, optoelectronics, and nanoelectronics, owing to their extraordinary electrical and optical properties. However, these materials still face several challenges, including limited light-matter interactions, low luminescent yield, reduced carrier mobility, and susceptibility to environmental changes. This thesis aims to address the aforementioned limitations by employing various advanced techniques to enhance the optical and electronic properties of these materials.

In this thesis, the light-matter interaction in TMDCs is enhanced by realizing mixed-dimensional heterostructures. High-performance photonic and optoelectronic devices are constructed by investigating two distinct types of these heterostructures. Firstly, monolayer MoS_2 is transferred onto AlGaAs nanowires to create a mixed-dimensional heterostructure. A significant enhancement in Raman and photoluminescence responses is achieved from the heterostructure attributed to the electromagnetic field confinement within the high refractive index nanowire. The heterostructure also exhibits optical anisotropy due to the 3-fold rotational symmetry breaking of MoS_2 caused by the nanowire. Additionally, the fabricated phototransistor using this heterostructure demonstrates improved responsivity and detectivity. Secondly, another mixed-dimensional heterostructure is formed by epitaxially growing InP nanowires directly on MoS_2. High-density nanowire growth is achieved while ensuring the stability of MoS_2. This heterostructure generates strong second- and third-harmonic signals and, notably, 5th and 7th-order high-harmonic signals, opening up potential applications such as lasers and electro-optic modulators.

In the subsequent part of the thesis, the electronic properties of TMDCs are investigated and tuned to fabricate high-performance electronic and optoelectronic devices. At first, the impact of high temperatures on multilayer $MoTe_2$ field-effect transistors is systematically explored to determine the optimal annealing temperature for the devices and acquire a deeper understanding of the surface oxidation-mediated defect formation and hopping transport mechanism in $MoTe_2$ devices. Furthermore, a straightforward technique is proposed that involves substrate engineering and Al_2O_3 passivation to enhance the performance of few-layer $MoTe_2$ devices by introducing local tensile strain and reducing electron-phonon scattering in the channel. This results in significant improvements in carrier mobility and device quality. Lastly, a simple optical writing technique is employed to transform the semiconducting 2H phase of $MoTe_2$ into the metallic 1T´ phase, resulting in improved third harmonic generation signals and the performance of optoelectronic devices. These findings show great promise for advancing integrated photonic and optoelectronic circuits based on 2D-TMDCs.

Keywords Two-dimensional materials, transition metal dichalcogenides, mixed-dimensional heterostructures, photoluminescence, harmonic generations, field effect transistors.

ISBN (printed) 978-952-64-1589-5 **ISBN (pdf)** 978-952-64-1590-1

ISSN (printed) 1799-4934 **ISSN (pdf)** 1799-4942

Location of publisher Helsinki **Location of printing** Helsinki **Year** 2023

Pages 123 **urn** http://urn.fi/URN:ISBN:978-952-64-1590-1

Preface

The research presented in this thesis was conducted in the Nanoscience and Advanced Materials group at the Department of Electronics and Nanoengineering under the supervision of Professor Harri Lipsanen.

First and foremost, I extend my sincere gratitude to Professor Harri Lipsanen for providing me with the opportunity to pursue my doctoral studies in this group. I appreciate his guidance, support, and thoughtful supervision throughout my study. I would also like to express my thanks to my thesis advisor David Mackenzie for ensuring a smooth start of my research and providing invaluable guidance during the initial phase of my doctoral studies. Furthermore, my deepest appreciation goes to Faisal Ahmed for his careful guidance during the latter half of my doctoral study. His encouragement and assistance were indispensable in initiating my journey into publishing scientific articles in the fields of electronics and photonics. I am also thankful to Professor Zhipei Sun for his instruction and collaboration in my photonics research works.

Moreover, I extend my heartfelt appreciation to all my colleagues who have contributed to create a positive working atmosphere and made this an enjoyable journey. In particular, I want to express my gratitude to Md Gius Uddin who has been a supporting colleague and a wonderful friend since the beginning of my study here. I would also like to convey my deepest thanks to Henry Fernandez for his mentorship and assistance in my research works. Additionally, I wish to acknowledge and thank Susobhan Das, Xiaoqi Cui, Xueyin Bai, and Petri Mustonen for engaging in numerous discussions regarding research matters and life in general.

Finally, I am eternally grateful to my wife, Razoana Hasanat, for her unwavering love and support during the challenging times of my studies. Her immense encouragement not only helped me overcome many research-related difficulties but also contributed to achieving a balance between my academic pursuits and family life.

Espoo, October 20, 2023

Abde Mayeen Shafi

Contents

Contents i

List of Abbreviations and Symbols iii

List of Publications v

Author's Contribution vi

1. Introduction **1**

2. Low-dimensional Materials **4**

2.1 0D and 1D materials 4

2.2 2D materials 6

2.3 2D vdW and mixed-dimensional heterostructures 7

3. Fundamentals of TMDCs **10**

3.1 Structure and electronic properties 10

3.2 Preparation methods 12

3.2.1 Mechanical exfoliation 12

3.2.2 Chemical vapor deposition methods 13

4. Methodologies **18**

4.1 Sample preparation techniques 18

4.1.1 Transfer of CVD-grown TMDCs 18

4.1.2 MOVPE growth of nanowires 19

4.1.3 Formation of 2D-1D heterostructures 19

4.1.4 Fabrication of 2D devices 21

4.2 Characterization techniques 22

4.2.1 Optical spectroscopies 22

4.2.2 Electron microscopies 24

4.2.3 X-ray photoelectron spectroscopy 25

4.2.4 Atomic force microscopy 26

4.2.5 Electrical measurements 27

4.2.6 Photocurrent measurements 30

5. 2D-1D Heterostructures for Photonics **31**

5.1 Enhancement of optical properties 31

5.1.1 Charge transfer and nanowire's confined field 33

5.2 Enhancement of optoelectronic properties 34

5.3 Nonlinear optics in epitaxially-grown heterostructures 35

5.3.1 Epitaxial growth of nanowires on TMDCs 36

5.3.2 Generation of nonlinear optical responses.............39

6. Tuning Electronic Properties of TMDCs 41

6.1 Effect of high-temperature treatment.................................41

6.1.1 Annealing and high-temperature impact.................41

6.1.2 Phase transition and surface oxidation 43

6.1.3 Hopping transport in $MoTe_2$ devices.......................44

6.2 Effect of strain and doping..45

6.2.1 Carrier mobility enhancement................................45

6.2.2 Polarity of strained $MoTe_2$ devices......................... 48

6.2.3 Metal-insulator transition 49

6.3 Phase modulation by optical writing..................................49

6.3.1 Influence on optical properties...............................49

6.3.2 Enhancement of optoelectronic properties............. 51

7. Conclusion 53

References 55

Publications 66

List of Abbreviations and Symbols

AFM	Atomic force microscopy
CNT	Carbon nanotube
C_{ox}	Capacitance of oxide
CVD	Chemical vapor deposition
D^*	Specific detectivity
EF	Enhancement factor
EM	Electromagnetic field
FET	Field effect transistor
GQD	Graphene quantum dot
hBN	Hexagonal boron nitride
HHG	High harmonic generation
HR-TEM	High-resolution transmission electron microscopy
HSA-CVD	Halide salt-assisted chemical vapor deposition
I_d	Drain current
I_{ON}/I_{OFF}	On-off ratio
I_{Ph}	Photocurrent
MIT	Metal-insulator transition
MOVPE	Metal-organic vapor phase epitaxy
MSA-CVD	Molten salt-assisted chemical vapor deposition
NW_{AlGaAs}	AlGaAs nanowire
NW_{InP}	InP nanowire
PL	Photoluminescence
PMT	Photomultiplier tube
R	Responsivity

R_{CH}	Channel resistance
R_{SH}	Sheet resistance
SA-CVD	Salt-assisted chemical vapor deposition
SAE	Selective area epitaxy
SBH	Schottky barrier height
SEM	Scanning electron microscopy
SHG	Second harmonic generation
TBP	Tertiarybutylphosphine
TEM	Transmission electron microscopy
THG	Third harmonic generation
TMDC	Transition metal dichalcogenides
TMIn	Trimethylindium
TMO	Transition metal oxide
V_d	Source-drain voltage
vdW	van der Waals
V_g	Gate voltage
VLS	Vapor-liquid-solid
VSS	Vapor-solid-solid
V_{th}	Threshold voltage
XPS	X-ray photoelectron spectroscopy
0D	Zero dimensional
1D	One dimensional
2D	Two dimensional
2PP	2-point probe
4PP	4-point probe
μ	Field effect mobility

List of Publications

This thesis consists of an overview of the following publications which are referred to in the text by their numerals.

I. **Shafi, A. M.**; Ahmed, F.; Fernandez, H. A.; Uddin, M. G.; Cui, X.; Das, S.; Dai, Y.; Khayrudinov, V.; Yoon, H. H.; Du, L.; Sun, Z.; Lipsanen, H. 2022. Inducing Strong Light–Matter Coupling and Optical Anisotropy in Monolayer MoS_2 with High Refractive Index Nanowire. *ACS Applied Materials & Interfaces*, 14 (27), 31140–31147.

II. **Shafi, A. M.**; Das, S.; Khayrudinov, V.; Ding, E.-X.; Uddin, M. G.; Ahmed, F.; Sun, Z.; Lipsanen, H. 2022. Direct Epitaxial Growth of InP Nanowires on MoS_2 with Strong Nonlinear Optical Response. *Chemistry of Materials*, 34 (20), 9055–9061.

III. Ahmed, F. †; **Shafi, A. M.** †; Mackenzie, D. M. A.; Qureshi, M. A.; Fernandez, H. A.; Yoon, H. H.; Uddin, M. G.; Kuittinen, M.; Sun, Z.; Lipsanen, H. 2021. Multilayer $MoTe_2$ Field-Effect Transistor at High Temperatures. *Advanced Materials Interfaces*, 8 (22), 2100950. †**Equal contribution**.

IV. **Shafi, A. M.**; Uddin, M. G.; Cui, X.; Ali, F.; Ahmed, F.; Radwan, M.; Das, S.; Mehmood N.; Sun, Z.; Lipsanen, H. 2023. Strain Engineering for Enhancing Carrier Mobility in $MoTe_2$ Field-Effect Transistors. *Advanced Science*, 2303437.

V. Ahmed, F.; Rodríguez-Fernández, C.; Fernandez, H. A.; Zhang, Y.; **Shafi, A. M.**; Uddin, M. G.; Cui, X.; Yoon, Mehmood N.; Liapis, A. C.; Yao, L.; Caglayan, H.; Sun, Z.; Lipsanen, H. 2023. Deterministic Polymorphic Engineering of $MoTe_2$ for Photonic and Optoelectronic Applications. *Advanced Functional Materials*, 8 (22), 2302051.

Author's Contribution

Publication I: Inducing Strong Light–Matter Coupling and Optical Anisotropy in Monolayer MoS_2 with High Refractive Index Nanowire.

The author came up with the research idea, designed the experiments, fabricated the samples, conducted all the major optical and electrical experiments, analyzed the data, and wrote the manuscript.

Publication II: Direct Epitaxial Growth of InP Nanowires on MoS_2 with Strong Nonlinear Optical Response.

The author came up with the research idea, designed the experiments, grew MoS_2, assisted in optimizing the parameters for growing heterostructures, analyzed the experimental data, and wrote the manuscript.

Publication III: Multilayer $MoTe_2$ Field-Effect Transistor at High Temperatures.

The author contributed equally to design the experiments and fabricate the devices, performed major electrical and material characterizations, and wrote the manuscript with the first co-author.

Publication IV: Strain Engineering for Enhancing Carrier Mobility in $MoTe_2$ Field-Effect Transistors.

The author came up with the research idea, designed the experiments, fabricated the samples, conducted all the major optical and electrical experiments, analyzed the data, and wrote the manuscript.

Publication V: Deterministic Polymorphic Engineering of $MoTe_2$ for Photonic and Optoelectronic Applications.

The author helped in performing material characterization (Raman spectroscopy and AFM) and the final revision of the manuscript.

1. Introduction

Graphene, a single layer of carbon atoms, made a great impact on the scientific community when it was first discovered in 2004[1]. This groundbreaking material achieved widespread attention due to its extraordinary properties, which include exceptional electrical conductivity, chemical inertness, and remarkable mechanical strength[2]–[4]. Layered transition metal dichalcogenides (TMDCs), another class of 2D materials, started gaining interest around the same time as graphene[5]. These materials offer a unique platform for exploring diverse electronic, optical, and mechanical properties. The history of TMDCs dates back to the early 20th century, however, researchers began to systematically investigate their intriguing properties in the early 21st century. The zero bandgap and absence of luminance in graphene led researchers to explore alternative or complementary materials within the 2D family. TMDCs gained significant attention due to their tunable bandgaps with relatively high luminescence. These properties make them highly desirable for advancing 2D research in electronics, optoelectronics, and photonics.[6]–[8] Their atomically thin nature, excellent semiconducting behavior, and strong light-matter interactions signify these materials with great potential. Nevertheless, despite these exotic properties, TMDCs still show certain limitations in their optical and electronic characteristics, which could pose challenges for their practical applications.

Atomically thin 2D layered materials like TMDCs have limited luminescence quantum yield due to defect-induced nonradiative recombination of electron-hole pairs and unlike their bulk counterparts, they have a very short interaction length between light and matter. Therefore, the performance of the photonic and optoelectronic devices based on TMDCs is hindered significantly.[9], [10] Various strategies have been employed to enhance light-matter interactions in 2D materials[11], [12], including integration with Fabry-Perot optical cavities[13], optical waveguides[14], plasmonic structures[15], and meta-surfaces[16]. Notably, plasmonic nanostructures constructed from noble metals like Ag and Au nanowires have demonstrated advanced capabilities in manipulating light-matter interactions in 2D materials. However, these structures and their fabrication processes are intricate and lead to optical losses caused by metals[17], [18]. They also face compatibility issues with semiconductor fabrication processes. Semiconductor nanowires with high refractive indices offer a novel and promising platform to address these challenges and enhance the functionality of 2D materials. For instance, the light-matter interactions and symmetry of monolayer 2D TMDCs like MoS_2 can be tuned by utilizing III-V

semiconductor nanowires such as AlGaAs to create mixed-dimensional heterostructures[19].

Additionally, III-V semiconductor nanowires have several advantageous properties including efficient light trapping, minimal crystal defects, material stability, and outstanding carrier mobility[20]–[23]. They also offer relaxed lattice matching requirements due to their small structure which makes the nanowires suitable for growing on various substrates, including ultrathin 2D materials like graphene and MoS_2[24]–[30]. Growing 1D nanowires on 2D TMDCs shows great potential in the creation of mixed-dimensional heterostructures, leading to the construction of high-performance photonic devices. However, the vertical growth of nanowires on 2D materials faces challenges due to limited nucleation sites resulting from the absence of dangling bonds on TMDCs. Moreover, ensuring the stability of TMDCs after nanowire growth is crucial for harnessing the advantages of mixed-dimensional heterostructures. III-V nanowires, such as InP, are a great choice for this type of heterostructures. They can be grown at relatively low temperatures, which is crucial for preserving the crystal stability of 2D materials like MoS_2 during the formation of the heterostructure. Furthermore, the mixed-dimensional heterostructures formed by InP nanowires and MoS_2 exhibit exceptional nonlinear optical characteristics[31].

In terms of electronic drawbacks, a key limitation of 2D TMDCs is their comparatively low charge carrier mobility. This limitation can hinder their performance in high-speed electronic devices. For instance, the mobility of $MoTe_2$ devices falls significantly below the theoretical limit of 200 $cm^2V^{-1}s^{-1}$ in practice[32]–[35]. Various strategies such as chemical doping, strain induction, and substrate engineering have been explored to enhance the performance of 2D-material-based devices[36]–[38]. Notably, ALD-grown Al_2O_3 is a high dielectric constant material (κ = 9.1) that can reduce the defects and charge trapping, induce n-type doping, and improve thermal and chemical stability in 2D materials[39]–[41]. Additionally, with appropriate substrate engineering, ALD-Al_2O_3 can induce tensile strain in $MoTe_2$ due to its weight and the difference in thermal expansion between Al_2O_3 and $MoTe_2$, further enhancing device performance[42].

Moreover, TMDCs can be sensitive to environmental conditions. Their response to temperature variations, humidity, and exposure to certain gases can impact their electronic properties. TMDC-based electronic devices typically operate at high ambient temperatures in a circuit due to several factors such as Joule heating, environmental conditions, and high-power dissipation density in compact circuits, and are subject to inevitable thermal stress[43]. Among other TMDCs, $MoTe_2$ is more prone to thermally induced structural defects. For instance, Te atoms in $MoTe_2$ dissociate at temperatures between 473 and 523 K[44], [45], resulting in chemically and electrically active defects that act as charge carrier traps to degrade field effect transistors (FET) performance[46]. Therefore, the thermal sensitivity of $MoTe_2$ necessitates careful consideration when subjected to temperature variations[47]. In general, most devices based on semiconducting 2D materials are more susceptible to high operating temperatures compared to their bulk counterparts due to their high surface-to-volume

ratio and poor thermal conductivity. Hence, it is crucial to investigate the behavior of emerging semiconducting 2D materials at high temperatures to design robust devices for practical conditions.

Researchers are actively working to address these optical and electronic limitations through various strategies. A concept gaining increasing interest in this pursuit is polymorphism, which refers to the presence of multiple crystalline structures with the same chemical composition in a material[48]–[50]. Polymorphism engineering in TMDCs has gained significant attention due to its ability to tailor material properties developing diverse electronic and optical devices, including transistors, photodetectors, meta-surfaces, and optical gratings[51]–[53]. Various techniques have been employed to change the crystal phases of materials, including epitaxial growth[54], lithography[55], chemical treatments[56], etc. However, they often suffer from limitations like non-uniformity, fabrication complexity, low quality and yield, and high instrumental cost. In contrast, optical patterning is promising due to its spatial selectivity, simplicity, and lithography-free approach that utilizes only a laser and lens setup[57], [58]. For instance, multilayer $MoTe_2$ with 2H phase can be simply transformed into 1T´phase using a visible laser that facilitates the creation of high-performance photonic and optoelectronic devices[59].

This thesis extensively explores the enhancement of both the optical and electronic properties of TMDCs. Chapter 2 provides brief definitions of various low-dimensional materials and their heterostructures. In Chapter 3, a comprehensive discussion of the fundamentals of TMDCs is presented. Chapter 4 explains the methodologies employed for the experiments such as sample preparation and characterization methods, and materials used. Enhancement of the optical and optoelectronic properties of TMDCs through mixed-dimensional heterostructures is presented in Chapter 5, Chapter 6 demonstrates the methods for tuning the electronic properties of TMDCs. Finally, the thesis is concluded in Chapter 7, summarizing the findings and prospective applications of TMDCs.

2. Low-dimensional Materials

Low-dimensional materials are characterized by their structural confinement in zero, one, or two dimensions. These materials exhibit unique properties due to their reduced dimensions, leading to numerous applications in nanotechnology, nanoelectronics, and many other fields. In this chapter, the definitions, and general properties of zero-, one-, and two-dimensional materials are presented. Additionally, a brief discussion about different two-dimensional van der Waals (vdW) structures and mixed-dimensional heterostructures is provided afterward, offering valuable insight into the perspective of these nanomaterials and their heterostructures in a wide range of applications.

2.1 0D and 1D materials

Nanomaterials having dimensions within the range of 1 nm to 100 nm in all directions are considered zero-dimensional (0D) materials. They include novel metal nanoparticles, magnetic nanoparticles, carbon quantum dots, graphene quantum dots (GQD), inorganic quantum dots, polymer quantum dots, and many more. 0D materials are particularly interesting due to their tunable optical and electrical properties, resulting from the quantum confinement effect.[60]

GQDs are significant exemplars of quantum dots, given that they are nanometer-sized fragments of graphene and exhibit distinct characteristics. Figure 2.1a shows a schematic of GQD with graphene crystal structure. The experimental and theoretical exploration of GQDs closely followed the research conducted on graphene. As graphene functions as a semiconductor with a zero bandgap and possesses infinite exciton Bohr diameter, the quantum confinement is observable in any fragment, although GQDs have dimensions below a diameter of 20 nm. The generation of GQDs involves fragmenting or "cutting" graphene sheets. However, chemical modifications have been applied to GQDs, leading to their applications in domains such as energy conversion, bioanalysis, and sensor technologies.[61]–[63]

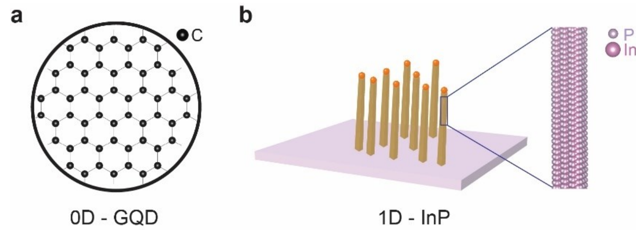

Figure 2.1. Examples of low-dimensional materials. Schematic of **(a)** GQD and **(b)** InP nanowires as examples of 0D and 1D materials, respectively. **(b)** is reproduced from **Publication II**.

Conversely, one-dimensional (1D) materials exhibit high length-to-diameter ratio. The most prevalent 1D materials are nanotubes, nanoribbons, and nanowires, and they hold promise for nanoelectronics and energy applications due to their unique structures and properties. Nanotubes, resembling cylinders at the nanoscale, possess superior abilities for efficient thermal and electric conductivity. For instance, carbon nanotubes (CNTs) are cylindrical structures composed of carbon atoms arranged in a hexagonal lattice, just like a rolled-up sheet of graphene[64]. These materials can be grown in single-walled and multi-walled forms, with single-walled CNTs consisting of just one layer and multi-walled CNTs containing concentric layers[65], [66]. CNTs have extraordinary mechanical strength, electrical conductivity, and thermal properties, making them ideal candidates for various applications, including nanoelectronics, composite materials, and energy storage[67].

Similarly, nanoribbons are ultra-thin ribbons that show excellent semiconducting properties. These nanoribbons are typically derived from layered materials like graphene or TMDCs, and their width can range from a few to tens of nanometers, while their length can extend up to micrometers. Due to their unique atomic structure and width-dependent electronic bandgap, nanoribbons possess tunable electrical properties, allowing precise control over their semiconducting behavior. Because of their unique properties, they can serve as key components in ultra-compact transistors, enabling the construction of high-performance, energy-efficient electronic circuits.[68], [69]

In contrast, nanowires are elongated nanostructures that exhibit exceptional electron mobility and radial quantum confinement[70]. In recent years, nanowires made from III-V semiconductors have gained considerable attention as highly prospective materials for a range of photonic and optoelectronic applications. This is primarily due to their direct band gap characteristics, uncomplicated and cost-effective production methods, and exceptional capacity for integration. Moreover, the capability to finely control doping of these nanowires enhances the tuning of electronic properties, further broadening their potential for innovative optoelectronic advancements. Because of these remarkable properties, they are seamlessly integrated into various devices, enhancing their versatility in applications like transistors, logic gates, lasers, modulators, photodetectors, and solar cells[71]–[73].

The most common method for growing these nanowires is metal-organic vapor phase epitaxy (MOVPE) which involves two growth modes: masking- and

kinetics-based selective area epitaxy (SAE), and droplet-directed vapor-liquid-solid (VLS). These modes enable precise control of nanowire characteristics like length, diameter, composition, crystal structure, and doping. In SAE growth process, the material's growth occurs in predefined masked areas. Nanowire growth using this process facilitates various axial and radial heterostructures and doping profiles, offering unique opportunities for nanophotonics applications. VLS growth involves vapor-phase species collecting at a droplet, catalyzing the growth of the semiconductor crystal from the droplet's surface. Key materials for VLS nanowire growth include GaAs, GaP, InP, InAs, and their ternaries, resulting in both zinc blende and wurtzite crystal structures[74], [75]. Figure 2.1b shows a schematic of InP nanowires grown on Si substrates using VLS method. The inset of the figure exhibits the crystal structures of the InP nanowire.

2.2 2D materials

2D materials consist of a single or a few atomic layers of solid crystals, exhibiting two dimensions significantly larger than the third, and result in a flat and sheet-like structure. Starting with graphene and extending to TMDCs, these materials have attracted significant interest recently because of their exceptional electrical, optical, and mechanical properties. They are considered to possess great potential in the fields of electronics, photonics, and flexible and transparent devices.

Graphene is a single layer of carbon atoms organized in a hexagonal honeycomb lattice structure. It has captured immense scientific and technological interest after its discovery in 2004[76]. Its remarkable properties such as exceptional electrical conductivity, mechanical strength, and thermal conductivity. These properties make graphene a versatile material for many applications. Graphene's unique electronic structure gives rise to intriguing quantum effects, making it a potential candidate for next-generation electronics, transparent conductors, and high-performance sensors. Additionally, its impermeability to gases and large surface area make it a potential material for applications in energy storage and filtration systems. Ongoing research seeks to harness graphene's extraordinary qualities for advancements in nanoelectronics, nanophotonics, and composite materials.[77]

Figure 2.2a shows the hexagonal honeycomb lattice of graphene on a 2D plane, in which the neighboring carbon atoms are covalently bonded by each other. Regarding its electronic characteristics, graphene can be described as a semi-metallic semiconductor with zero bandgap. This is because of the convergence of its conduction and valence bands at Dirac points. In Figure 2.2b, the conduction band (denoted as π^* band) and the valence band (π band) intersect at six specific points, located at the periphery of the hexagonal Brillouin zone [78].

Hexagonal boron nitride (hBN) is another unique 2D layered material. It consists of boron and nitrogen atoms, held together by covalent bonds in a honeycomb lattice-like graphene, as shown in Figure 2.2c[79]. With a wide bandgap

of approximately 5.8 eV, hBN behaves as a layered insulator. The band structure of monolayer hBN is presented in Figure 2.2d. Its atomically thin layers have a pristine surface, free from dangling bonds and charge carrier traps, making it distinctive from the bulk insulating materials like SiO_2, Al_2O_3, and HfO_2 that

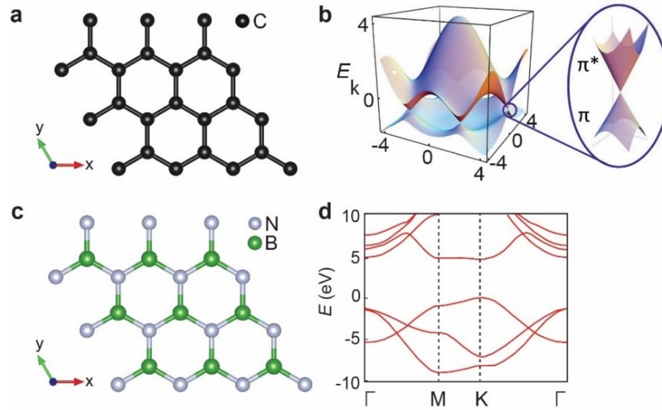

Figure 2.2. Fundamental characteristics of 2D materials. **(a)** Schematic of the crystal structure of graphene. **(b)** Electronic dispersion in the graphene lattice. At six Dirac points, the conduction band meets the valence band (on the left), and a clearer representation of the energy bands at the Dirac point (on the right).[78]. **(c)** Crystal structure of hBN. **(d)** Band structure of monolayer hBN[80].

show increase in surface roughness and defects upon scaling down. hBN has a dielectric constant of 3.5 and higher phonon energies (~ 200 meV) than conventional SiO_2 (60–80 meV)[81]. Additionally, hBN provides mechanical robustness, remarkable thermal conductivity, high optical transparency, and chemical stability even when the material is scaled down to its monolayer dimension[82]. These properties make hBN a prospective material for ultrathin gate dielectric, showing potential in flexible and transparent miniaturized devices[83].

TMDCs have become a prominent class of 2D layered materials, attracting immense interest following graphene. Their unique atomic arrangements and tunable properties make them compelling materials for a wide range of applications. This thesis primarily focuses on TMDCs and their associated heterostructures. More details on TMDCs are provided in the subsequent chapter.

2.3 2D vdW and mixed-dimensional heterostructures

2D vdW heterostructures have emerged as a cutting-edge platform for engineering layered material functionalities with improved characteristics. They are created by stacking various 2D materials on top of one another and held together with weak vdW forces.[84], [85] The electronic, optical, and mechanical behaviors of these heterostructures can be precisely controlled and refined since they combine distinct material properties of each constituent material. For instance, stacking graphene with TMDCs can result in heterostructures with tunable bandgaps, making them useful for optoelectronic and sensing applications. The twisted bilayer graphene, which consists of two layers of graphene rotated at a specific angle with respect to one another, is another well-known example of a

2D vdW heterostructure[86]. This twisting angle can result in unconventional superconductivity by creating flat electronic bands and the generation of moiré patterns. Additionally, MoS_2 and WSe_2 exhibit intriguing interlayer exciton effects and optical properties when they are stacked together[87]. Overall, 2D vdW heterostructures offer great potential for advancing fields such as electronics, photonics, and quantum technologies[88]. Figure 2.3a shows the schematic of vdW heterostructures formed with different 2D materials.

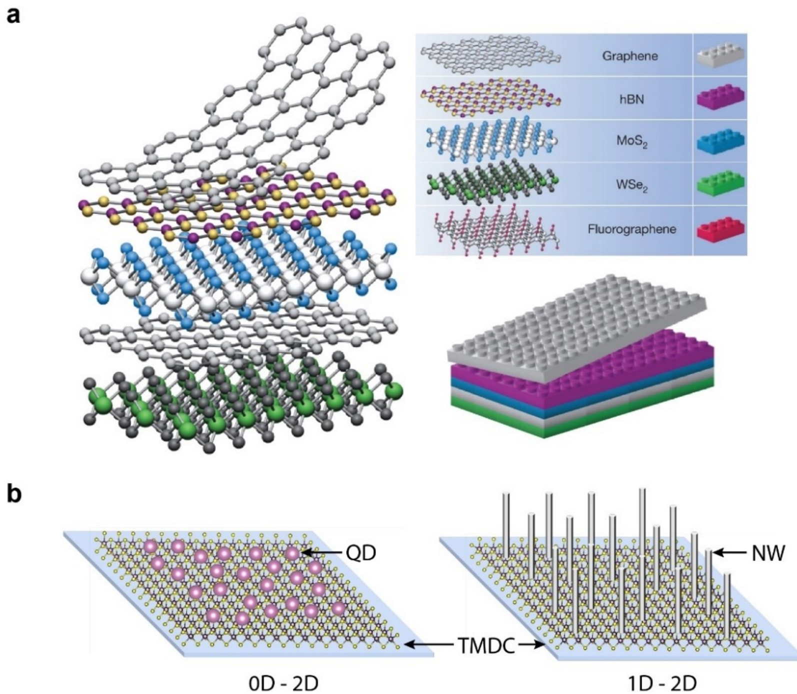

Figure 2.3. Schematic of different types of heterostructures. **(a)** 2D vdW heterostructures[84]. **(b)** Mixed-dimensional heterostructures with TMDC and quantum dot (QD) in the left panel and nanowires (NW) in the right panel.

In contrast, mixed-dimensional heterostructures combine materials of different dimensionalities, such as 0-, and 1- materials with 2D materials, which have gained significant interest recently because of their ability to enhance the properties of the materials for many new applications[89]. In 2D-0D heterostructures, the 2D material (Graphene, hBN, TMDCs, etc.) interfaces with 0D nanostructures (QD, nanoparticles, etc.). These heterostructures are also held together by vdW force and their interaction leads to quantum confinement effects in the quantum dots and modified electronic properties in the 2D materials[90], [91]. These heterostructures have applications in nanoelectronics, photonics, and quantum information processing due to their tunable electronic and optical properties.

2D-1D heterostructures are another fascinating combination, in which 2D materials interact with 1D nanowires, nanoribbons, or nanotubes.[30] For example, combining a 2D semiconductor like TMDCs with 1D metallic, semiconducting, and dielectric nanowires can yield efficient charge transport, electric field

confinement, and light-matter interaction[19], [92]–[94]. This type of heterostructure design has applications in high-performance sensors, photodetectors, and flexible electronic devices. Another example is the integration of TMDC monolayers with metallic nanowires to create ultrasensitive photodetectors capable for detecting even minute amounts of light due to the enhanced light absorption in the 2D layer and efficient charge transport through the nanowires[95]. Mixed-dimensional heterostructures, create exciting avenues for tailoring material functionalities and designing devices with enhanced performance.

3. Fundamentals of TMDCs

TMDCs have emerged as one of the most extensively studied materials since the discovery of graphene. These 2D materials exhibit remarkable properties due to their distinctive electronic and optical characteristics. This study is primarily based on TMDCs, therefore, a detailed discussion on their structural and electronic properties, and preparation methods are presented in this chapter.

3.1 Structure and electronic properties

TMDCs are a family of 2D semiconducting materials composed of transition metal atoms (e.g., Mo, W, Re, and so on) sandwiched between chalcogen atoms (sulfur, selenium, or tellurium) in a layered structure. The compound material can be represented as MX_2, with M and X denoting transition metals and chalcogen atoms, respectively. Figure 3.1a illustrates a periodic table, presenting M and X's atoms enclosed within blue and red boxes, respectively. TMDCs possess a finite band gap, making them valuable for electronics and optoelectronics applications. TMDCs exhibit a range of properties, including strong light-matter interactions, making them promising candidates for photodetectors, light-emitting diodes, and solar cells. The ability to tune their electronic properties through strain, doping, or layer stacking offers opportunities for designing devices with tailored functionalities. TMDCs have also shown potential for novel quantum phenomena, such as the creation of excitons and valleytronics effects.

TMDCs exhibit several structural polymorphs that significantly influence their properties and potential applications[5]. These polytypic configurations include 2H, 1T, and 1T′ phases as depicted in Figure 3.1b. The 2H phase, typically semiconducting, features a single XMX monolayer with a Bernal (ABA) atomic stacking sequence and trigonal prismatic M-X coordination. In contrast, the 1T phase adopts a rhombohedral (ABC) stacking pattern, with atoms forming an octahedral arrangement. Although the 1T phase is metallic, its susceptibility to Peierls distortion leads to the formation of the 1T′ phase, resulting in distorted octahedral coordination between atoms. While the 2H phase is generally thermodynamically stable in most combinations of MX_2 monolayers, the semi-metallic 1T′ phase often exists in a metastable state in other TMDCs[96], [97].

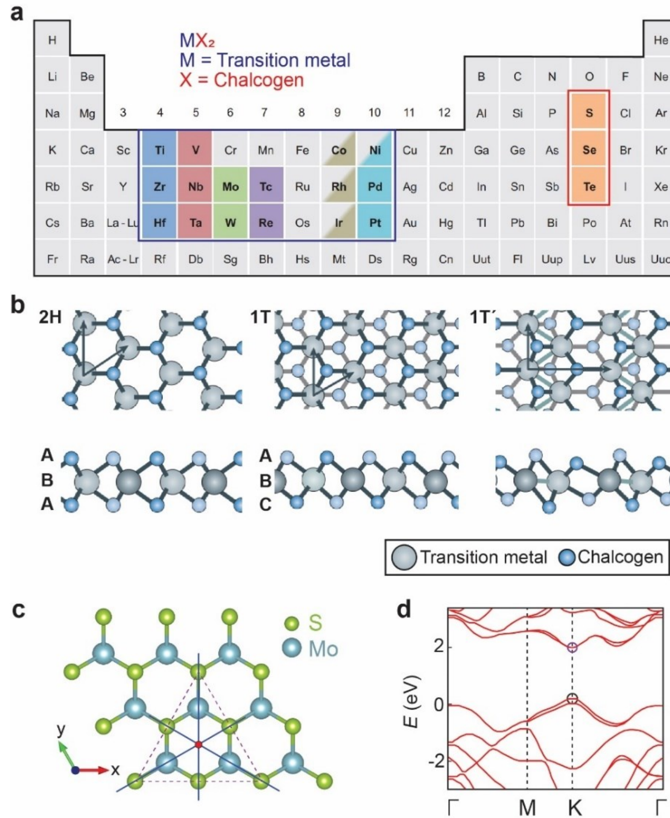

Figure 3.1. Fundamental properties of TMDCs. **(a)** Periodic table showing transition metals (denoted as M) within the blue box and chalcogen (X) within the red box. M and X elements form MX_2, known as TMDC. **(b)** 2H, 1T and 1T′phases of $MoTe_2$ crystal from top and side view[5]. **(c)** MoS_2 crystal structure. The blue lines denote mirror reflection planes, while a red circle positioned at the triangle's center represents the crystal's axis of 3-fold rotational symmetry. **(d)** Schematic representing the band structure of a monolayer of MoS_2, where the two circles at the *K* point highlight the direct bandgap[98]. **(c)** is reproduced from **Publication I**.

Notably, $MoTe_2$ is one of the unique TMDCs due to its minimal energy difference (40 - 50 meV) between the 2H and 1T′ phases. This feature enables relatively easy phase transitions from 2H to 1T′ and vice versa. Modulating $MoTe_2$'s polymorphism can be effectively achieved through precise control of growth temperature and post-growth cooling processes. Furthermore, techniques such as laser irradiation, selective ion, and electron beam exposure, oxidation, and plasma treatment have been reported as efficient methods for inducing phase conversion in $MoTe_2$.[59], [99]

Among the family of TMDCs, MoS_2 has been the most studied material in the last decade. The monolayer MoS_2 possesses a noncentrosymmetric unit cell, belonging to the nonpolar D_{3h} point group. Along the armchair direction, the crystal exhibits mirror reflection and 3-fold rotational symmetries. These symmetries play an important role in influencing the material's electronic and optical responses. Figure 3.1c presents a 2H-MoS_2 crystal structure with blue lines and the red circle representing a mirror reflection plane and a rotational symmetry axis, respectively. Furthermore, the bandgap of MoS_2 exhibits sensitivity to

changes in layer thickness. In multilayer MoS_2, the bandgap is approximately 1.2 eV. However, as the thickness decreases to a monolayer, the bandgap increases to around 1.8 eV. Notably, the decreasing thickness of MoS_2 leads to a transition from an indirect to a direct bandgap when it becomes a monolayer.[100][101] This intriguing behavior highlights the significant impact of dimensionality on the electronic properties of MoS_2, making it a promising material for various photonics and optoelectronic applications. Figure 3.1d shows the band structure of monolayer MoS_2 with two open circles located at the K point indicating the existence of a direct band gap within the material.[102]

3.2 Preparation methods

There have been several methods developed over the years to prepare TMDCs for photonics and electronic applications. However, this study primarily focuses on the preparation of these materials by mechanical exfoliation and chemical vapor deposition (CVD) processes. These methods are discussed in the following sections.

3.2.1 Mechanical exfoliation

The mechanical exfoliation process is a fundamental technique for isolating thin layers of 2D materials from their bulk counterparts.[1] This method, which has been widely used in research and development, involves manually peeling layers of a bulk crystal to obtain individual monolayer or few-layer flakes. The process is often referred to as the "Scotch tape method" due to the use of adhesive tapes to achieve the exfoliation.

In this process, a chemical vapor transport-grown bulk TMDC crystal, such as MoS_2, is firmly pressed on a piece of adhesive tape and then gently peel off the thin layers from bulk vdW materials. By carefully folding the tape several times, it becomes possible to isolate thinner layers, including monolayer flakes, which consist of just one layer of atoms. The flake is then transferred to the desired substrate for further analysis.

The mechanical exfoliation process requires a combination of techniques and patience. Finding monolayer flakes among multilayers can be challenging, and it often takes multiple attempts to obtain the desired flake. To improve the efficiency of the process, modified approaches have been developed, such as polymer film-assisted exfoliation[103], thin Au coating on the substrate[104], and hot pick-up technique[105]. These methods lead to the isolation of large area and high-quality monolayer flakes.

While mechanical exfoliation remains a powerful tool for producing pristine monolayer TMDCs with minimal introduction of defects, its limitations include low yields and challenges for large-scale production. Nevertheless, it is a crucial method for academic research and exploration of the intrinsic properties of TMDCs, providing insights into their unique characteristics and potential applications in various sectors like electronics, nanophotonics, and optoelectronics.

3.2.2 Chemical vapor deposition methods

CVD is a technique involving the chemical reaction of gaseous precursors to form a thin film on a substrate. It's widely employed in the production of various 2D materials like graphene, TMDCs, and other layered materials, primarily due to its capability for large-scale, high-quality material synthesis. The unique advantage of CVD process lies in its ability to precisely control the growth conditions, including temperature, pressure, and precursor flow rate, resulting in consistently uniform and homogeneous films, which are essential for many applications of 2D materials. Another advantage of CVD for 2D materials is its scalability. CVD can be used to grow 2D materials on a number of different substrates such as metals, semiconductors, and even flexible substrates. This makes it possible to integrate 2D materials into a wide range of devices, e.g., transistors, sensors, photodetectors, and solar cells.

Recently, the CVD method has emerged as a sophisticated alternative for effectively growing 2D TMDCs following graphene. This technique has proven successful in producing a range of atomically thin layered semiconductors, including MoS_2, WS_2, $MoSe_2$, and $MoTe_2$, among others. Several factors influencing the growth of 2D materials have been extensively investigated over the years, including parameters like growth temperature, carrier gas selection, source-substrate distance, and precursor supply. These variables have a significant impact on controlling nucleation density, vapor transport rate, growth rate, and overall morphology of the growth material. In the course of CVD growth, although each parameter has its primary role, they are interdependent and interact synergistically. Therefore, to achieve precise and controlled growth of 2D materials, a comprehensive consideration and design of all these growth parameters are needed. To date, several CVD techniques have been employed for growing large-area, defect-free, and highly crystalline TMDCs. In this study, both conventional and salt-assisted CVD methods have been employed to prepare the TMDCs. A detailed discussion about these methods is provided in subsequent sections.

Conventional chemical vapor deposition

Usually, a conventional CVD system for growing TMDCs includes a CVD furnace with 2 or 3 different temperature zones, a quartz tube, a control system, a vacuum pump, a mass flow control unit, and a pressure gauge. A schematic is presented in Figure 3.2 with all the basic components of a CVD system. In this technique, a transition metal oxide (TMO) powder containing aluminum crucible with the substrate is carefully placed in the high-temperature central region (heating zone 1), while a chalcogen powder containing crucible is placed upstream in the low-temperature region (heating zone 2). This strategic arrangement allows the precursor materials to react in a controlled manner, leading to the deposition of TMDC monolayers on the growth substrates. The growth process initiates with the vaporization of the TMO and chalcogen powders at sufficiently high temperatures. These vapors are transported by an inert carrier gas and guided onto the growth substrates. This process allows the precursor materials to reach the substrate surface where they chemically react. These reactions due to the optimized growth conditions with appropriate temperature,

pressure, and precursor flow rates result in the growth of TMDC monolayers on the substrate. The interaction between the vapor-phase precursors and the substrate is vital in determining the quality, uniformity, and morphology of the resulting TMD layers.

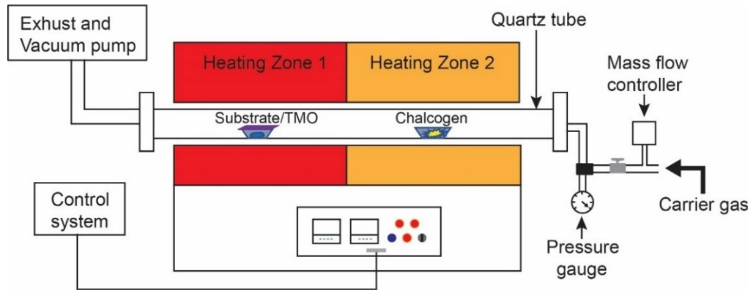

Figure 3.2. Schematic of a conventional CVD system for growing TMDCs.

In the conventional CVD process for MoS_2 growth, a crucible with MoO_3 powder and sulfur (S) powder is placed in high- and low-temperature regions, respectively, while growth substrate (SiO_2, Au, Mica, Sapphire, etc.) is placed on or next to the MoO_3 crucible positioned within that region. The growth is usually carried out at low- or atmospheric pressure. Vaporization of MoO_3 occurs at ~ 750 – 850 °C and ~ 180 °C for S powder[106]–[109]. Ar or a mixture of Ar and H2 is usually used as a carrier gas to transport these vapors to the substrates, leading to a chemical reaction that results in the formation of MoS_2 monolayers or few-layers on the substrate surface depending on the optimization of the growth conditions. This process is also referred to as the vapor-solid-solid (VSS) method. The chemical reaction for growing MoS_2 in conventional CVD can be expressed by the following equation[110]:

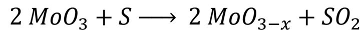

$$2\,MoO_3 + S \longrightarrow 2\,MoO_{3-x} + SO_2$$

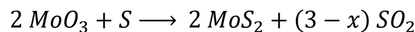

$$2\,MoO_3 + S \longrightarrow 2\,MoS_2 + (3-x)\,SO_2$$

Conventional CVD is an effective method for many applications. However, the process faces certain challenges and limitations. One significant challenge in the conventional CVD process is the low material yield. The small sizes of the grown 2D crystals hinder the wafer-scale production of TMDCs for industrial applications. Researchers have explored many techniques to address these issues such as oxygen-assisted growth[111], substrate engineering[112], the use of seeding promoters[109], plasma-treated substrate[107], and so on. Another effective process example is the "salt-assisted growth" which involves introducing iodine or chloride salts during the CVD process. These compounds act as catalysts, promoting larger crystal growth and enhancing material yield. Other strategies include optimizing precursor ratios, fine-tuning growth parameters, and exploring novel substrate designs to improve crystal size and quality. Despite these efforts, achieving large-area, high-quality 2D materials remains an ongoing focus in the field which are crucial for enabling their broader application in diverse technological areas.

Salt-assisted chemical vapor deposition

Salt-assisted CVD (SA-CVD) has emerged as a promising approach for the growth of large area and high-quality TMDCs. This method involves the halide and molten salts, during the CVD process to enhance crystal growth and improve material quality[113]–[115].

In Halide salt-assisted CVD (HSA-CVD) halide salts, alkali metal halides (e.g., NaCl, KBr, KI, etc.) play a crucial role as growth promoters. These halides are mixed with TMOs (e.g., MoO_3, WO_3, SnO_2, etc.) and form metal oxyhalides (e.g., $WOCl_4$, MoO_2Cl_2, etc.) and vaporize when heated above 600 °C. These metal oxyhalides, having low melting points (< 300 °C), serve as highly effective volatile precursors for the growth of high-quality TMDC monolayers on the substrate through the vapor-solid-solid (VSS) process. Meanwhile, the alkali metals such as Na or K also react with TMOs to create non-volatile molten salts (e.g., $Na_2Mo_2O_7$, $NaWO_3$, etc.), which subsequently react with chalcogen vapor, leading to the growth of TMDCs in a VLS process. Note that, both the volatile and non-volatile precursors are transported to the substrate in the vapor phase before initiating any VSS or VLS growth.

This process was first demonstrated by S. Li et al., in which they successfully grew a large area of WS_2 and WSe_2 at atmospheric pressure[113]. One major advantage of HSA-CVD is the ability to achieve WSe_2 growth at significantly lower temperatures (~ 700 °C) when mixed with KI. The growth temperature is ~ 100 °C lower than the conventional CVD method that relies solely on tungsten oxide. The TMDC monolayers grown using this method exhibit good quality. They are free from contamination when properly rinsed and transferred, and demonstrate excellent electronic properties, making them suitable for applications such as field-effect transistors.

The possible reaction for growing MoS_2 and WSe_2 using HSA-CVD is given below:

MoS_2:

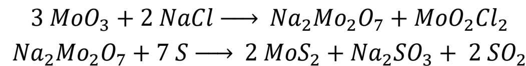

$$3\,MoO_3 + 2\,NaCl \longrightarrow Na_2Mo_2O_7 + MoO_2Cl_2$$
$$Na_2Mo_2O_7 + 7\,S \longrightarrow 2\,MoS_2 + Na_2SO_3 + 2\,SO_2$$

WSe_2:

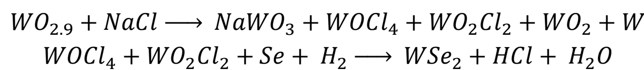

$$WO_{2.9} + NaCl \longrightarrow NaWO_3 + WOCl_4 + WO_2Cl_2 + WO_2 + W$$
$$WOCl_4 + WO_2Cl_2 + Se + H_2 \longrightarrow WSe_2 + HCl + H_2O$$

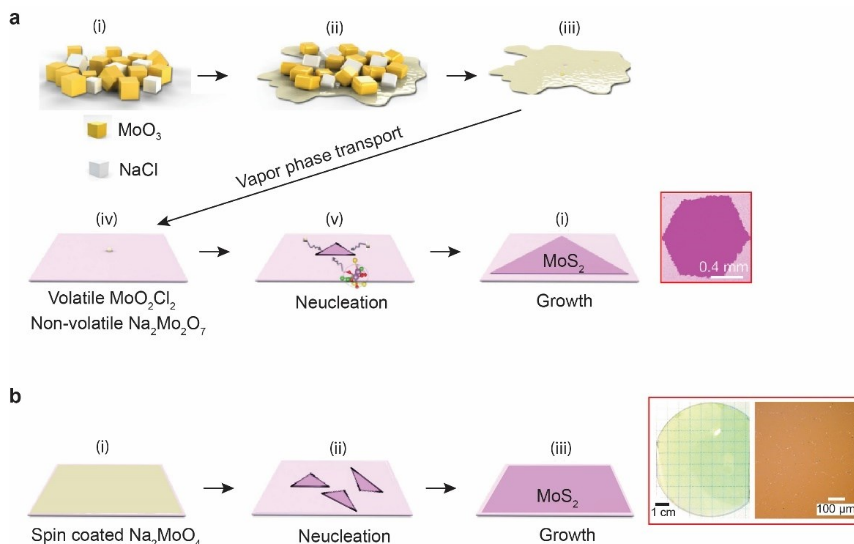

Figure 3.3. Growth mechanism of HSA-CVD and MSA-CVD methods. **(a)** Schematic of the steps of HSA-CVD process for growing MoS_2 monolayer crystal. The image in the red box is the optical image of HSA-CVD-grown large area MoS_2.[114] **(b)** Steps for growing MoS_2 in the MSA-CVD process. The actual optical image of wafer scale MoS_2 film grown using this method is shown inside the red box.[116]

An example of the HSA-CVD process for growing MoS_2 is presented in Figure 3.3a. The HSA-CVD method has been used for growing several kinds of metal chalcogenides and their alloys[117]. However, achieving wafer-scale and patterned growth of TMDCs is challenging due to some issues like the non-inform precursor distribution, poor coverage and reproducibility, and growth chamber contamination. These drawbacks can be overcome by the molten salt-assisted CVD (MSA-CVD) technique for growing large-scale and high-quality TMDCs.[118], [119]

In contrast to the complex growth modes of HSA-CVD, in which both VSS and VLS processes are involved, the MSA-CVD technique involves only the VLS growth mode[116]. In this method, molten salts (e.g., Na_2MoO_4, Na_2WO_4, etc.) are used to facilitate the growth of TMDCs. The precursors of HSA-CVD usually have relatively high melting points and create stable melts at low vapor pressure to ensure VLS growth. They are also soluble in water which makes them suitable to spin or drop coat on the growth substrates.

Na_2MoO_4 and Na_2WO_4 are commonly used precursors for growing Mo- and W-based TMDCs in the MSA-CVD process. In this method, the precursors in an aqueous solution are spin-coated onto hydrophilic growth substrates. This allows control over surface coverage, crystal domain size, and the number of layers. Large-scale growth of monolayer MoS_2 and WS_2 onto sapphire, SiO_2/Si, and other substrates has been achieved using this approach.

In the case of MoS_2 monolayer growth using the MSA-CVD method, spin-coated Na_2MoO_4 is melted at ~ 750 – 800 °C temperature to form stable Na_2MoO_4 melts on SiO_2/Si substrates[116]. The melts react with the sulfur vapor and solid monolayers of MoS_2 precipitate from the sulfur-saturated Na-Mo-O-S. Depending on the concentration of Na_2MoO_4 in the solution and the S

vapor supply, either large crystals or uniform films of monolayer MoS_2 can be achieved.

Figure 3.3b shows the MSA-CVD growth of monolayer MoS_2 on sapphire. While this technique has been successfully applied to grow transition metal sulfides, the growth of selenides and tellurides is in an early stage of development due to the challenge for finding suitable precursors. This method also requires relatively high temperatures for melting the salt and growing TMDCs, which is considered to be another major drawback.[120]

In this study, monolayer and few-layer MoS_2 are synthesized on SiO_2/Si substrate in the MSA-CVD process using Na_2MoO_4 and sulfur powder precursors. Initially, a solution of Na_2MoO_4 having 5 - 10 mg ml^{-1} density is spin-coated on mild oxygen-plasma treated SiO_2/Si substrate at 4000 rpm for 1 minute. The growth is performed in a separately controllable dual-zone CVD furnace, as shown in Figure 3.2. The quartz tube's dimensions are 50 mm in diameter and 200 cm in length. In the tube, ~ 100 mg sulfur powder is loaded on an aluminum boat and placed in the low-temperature zone. Simultaneously, the substrate coated with Na_2MoO_4 is positioned in the higher-temperature region. The temperature in the low and high-temperature zone is maintained at 180 °C and 750 - 800 °C, respectively. 70 - 100 sccm of Ar is used as carrier gas. The optimized growth duration is set at 10 minutes, after which the furnace naturally cools to room temperature. In this approach, 10-100 µm flakes of MoS_2 are successfully grown.

4. Methodologies

In this study, several methods are employed to investigate the properties of the fabricated photonic and electronic devices. This chapter focuses on sample preparation, material, and device characterization methods.

4.1 Sample preparation techniques

4.1.1 Transfer of CVD-grown TMDCs

To fabricate photonic and electronic devices on a desired substrate, TMDCs must undergo either a dry transfer or wet transfer process. The dry transfer involves exfoliating TMDCs onto a substrate, while CVD-grown TMDCs need the wet transfer method to transfer them from the growth substrate onto the desired substrate, since fabricating devices on the growth substrate can sometimes be challenging. Specifically, during MSA-CVD growth of TMDCs on a SiO_2/Si substrate, metal atoms like Na or K can make trenches on the SiO_2 during the growth process, leading to high gate leakage if transistor electrodes are made using a metal evaporation technique. Thus, to avoid gate leakage, it is important to transfer CVD-grown TMDCs onto a fresh substrate for device fabrication.

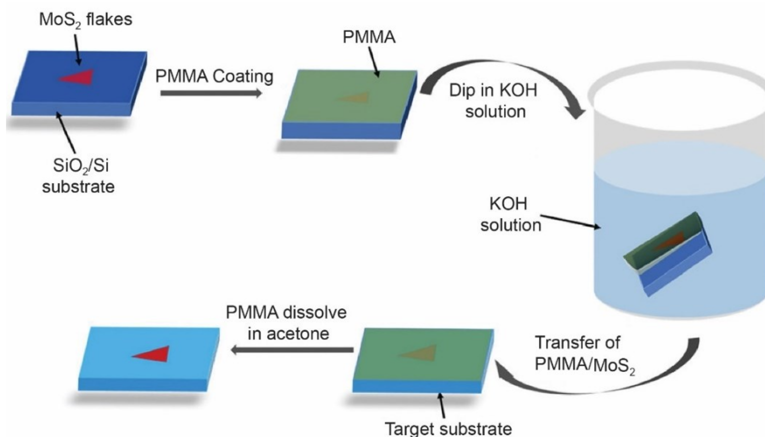

Figure 4.1. Schematic of a wet transfer process steps for transferring MoS_2 from a growth substrate to another substrate[121].

Typically, in a wet transfer process, 2 layers of 4.5 % w/w polymethyl methacrylate in anisole (PMMA A4.5) or 1 layer of PMMA A9 is initially spin-coated at

4000 rpm for 1 minute onto the SiO_2/Si growth substrate with TMDC flakes, followed by baking of the sample for 2 minutes at 160 °C on a hot plate. Subsequently, the coated substrate is immersed in a 45 % w/w potassium hydroxide solution (KOH) solution for dissolving SiO_2 until the PMMA/flakes layer detaches from the substrate and floats on the solution. After rinsing with deionized (DI) water, the PMMA/flakes layer is then transferred onto the desired substrate and allowed to dry in the air. Lastly, PMMA is dissolved in acetone, only flakes remain on the substrate. A wet transfer process is illustrated in Figure 4.1, in which MoS_2 flakes are transferred from a SiO_2/Si growth substrate to another substrate.

4.1.2 MOVPE growth of nanowires

MOVPE is a commonly used technique for growing III-V semiconductor materials with high precision and control. This method is based on the principle of chemical reactions of metal-organic precursors taking place in a vapor-phase environment to deposit thin semiconductor layers on a substrate. In this study, the III-V semiconductor nanowires (AlGaAs and InP) are also grown in the MOVPE process. The droplet directed VLS growth mode is used for growing the nanowires onto different substrates. In this process, metallic nanoparticles (commonly Au) in a colloidal solution are drop-casted onto the substrate. The vapor-phase precursors accumulate at the droplet during the growth process in an MOVPE reactor. Under appropriate growth conditions, the precursors nucleate and initiate solid nanowire growth beneath the droplet. As the nanowire grows, it elevates the droplet while the droplet remains on top of the nanowire.[122] By appropriately modifying the growth parameters, it is possible to inhibit axial nanowire growth and promote radial growth. A schematic of the process is shown in Figure 4.2.

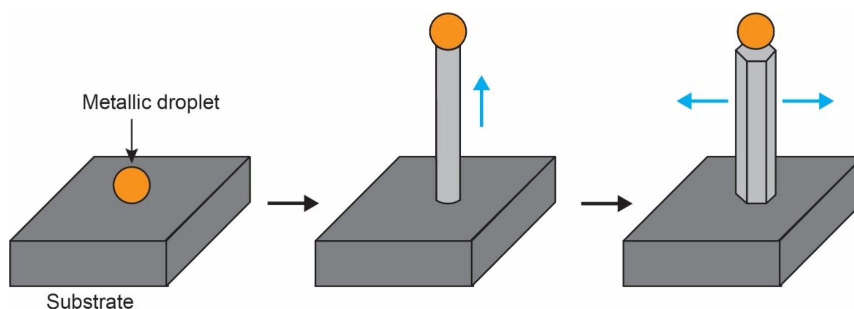

Figure 4.2. Schematic of a droplet directed VLS growth of III-V nanowires[122].

4.1.3 Formation of 2D-1D heterostructures

In this study, the properties of two types of mixed-dimensional heterostructures are investigated. Firstly, 2D MoS_2 and 1D AlGaAs nanowires (NW_{AlGaAs}) are combined to create mixed-dimensional heterostructures, aimed at enhancing the optical and optoelectronic characteristics of MoS_2 through the utilization of nanowires' electric field confinement properties. To assemble the

heterostructure, NW_{AlGaAs} are transferred on a SiO_2/Si substrate utilizing the nanocombing approach[123]. Following this, MSA-CVD-grown MoS_2 flakes are transferred onto the NW_{AlGaAs}/SiO_2/Si sample via a wet transfer process. The nanowires used in this investigation typically exhibit diameters of ~ 80–150 nm. Upon transferring monolayer MoS_2 onto NW_{AlGaAs}, MoS_2 covers the NW_{AlGaAs}, leaving a small suspended area near the bottom facets of NW_{AlGaAs}. Figure 4.3a depicts a schematic of the MoS_2/NW_{AlGaAs} heterostructure.

Other mixed-dimensional heterostructures are created by growing InP nanowires (NW_{InP}) on CVD-grown MoS_2. The heterostructures are grown in a horizontal flow MOVPE reactor at atmospheric pressure [26], [123]. Au nanoparticles with a diameter of 40 nm are utilized from a colloidal solution as catalysts. Prior to the Au nanoparticles spin coating, a solution of Poly-L-Lysine (PLL) is applied to the substrate with MoS_2 flakes to enhance the particles' adhesion to the substrate. Trimethylindium (TMIn) and tertiarybutylphosphine (TBP) are the precursors used for the growth of NW_{InP}. To facilitate nanowire growth, the precursors are simultaneously introduced into the reactor for 300 seconds, while maintaining 430 °C temperature in the reactor. The nominal V/III ratio is around 200, achieved by adjusting the TMIn and TBP flow rates to 80 sccm and 100 sccm, respectively. Only hydrogen (H_2) is utilized as the carrier gas, and the total gas flow rate within the 1-inch reactor is approximately 5 $lmin^{-1}$ (slm). A schematic illustration of the NW_{InP}/MoS_2 heterostructure is shown in Figure 4.3b.

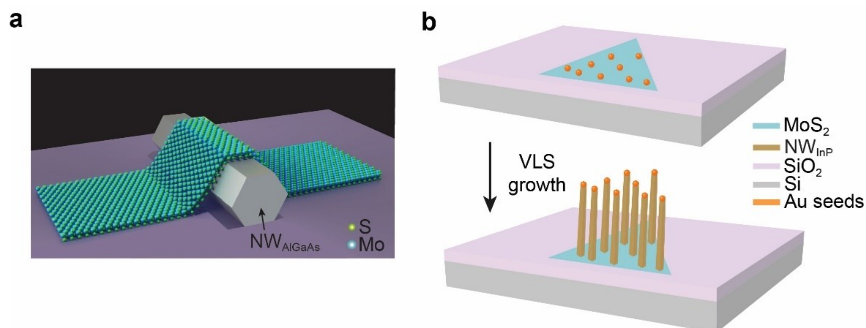

Figure 4.3. 2D and 1D material-based mixed-dimensional heterostructures. **(a)** Schematic of a MoS_2/NW_{AlGaAs} heterostructure. **(b)** Schematic of the Au-assisted VLS growth process of NW_{InP}/MoS_2 heterostructure. **(a)** and **(b)** are reproduced from **Publication I** and **II**, respectively.

4.1.4 Fabrication of 2D devices

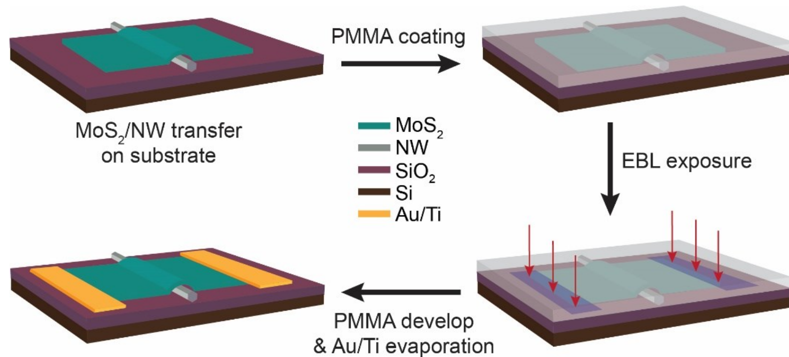

Figure 4.4. Schematic of the fabrication process steps for MoS_2/nanowire-based FETs.

FET is a voltage-controlled device with high input impedance. This is a fundamental component of modern semiconductor technology that supports a diverse variety of existing and emerging applications. 2D TMDCs emerge as another highly potential material for fabricating miniature FETs, offering exceptional electron mobility and electro-optic properties that pave the way for advanced nanoelectronic devices. In this study, TMDC-based FETs are meticulously fabricated using several nanofabrication techniques, ensuring precise control over the device parameters and performance. The process steps for fabricating a MoS_2/nanowire-based FET are illustrated in Figure 4.4.

Initially, III-V semiconducting nanowires are transferred onto a heavily p-doped silicon substrate coated with a layer of thermally grown SiO_2 that is 285 nm thick. Following this, CVD-grown or exfoliated MoS_2 is carefully transferred on top of the nanowires, creating mixed-dimensional heterostructures. After this step, PMMA A4.5 (positive resist) is spin-coated over the sample using a spinner at 2000 rpm for 60 seconds. This results in a PMMA layer of approximately 300 nm in thickness on the sample. The coated sample is then heated to 160 °C on a hot plate for 2 minutes. Electron beam lithography is carried out afterward to make electrodes on MoS_2. The electron beam is operated at a dose of 1000-1200 μCcm^{-2} and a current of 1-10 nA. These electrodes are created by exposing specific areas with an electron beam, creating openings after the PMMA is developed using a solution of MIBK (methyl isobutyl ketone) and IPA (isopropyl alcohol) in a 1:3 ratio.

The metallization process involves the deposition of a 5 nm thick layer of titanium (Ti) followed by a 50 nm thick layer of gold (Au). This deposition is carried out using an electron beam evaporator (MASA, IM-9912 model) within a vacuum chamber under a pressure of approximately 10^{-7} torr. The sample is then immersed in acetone for 2 hours to facilitate the lift-off process. All these individual steps are meticulously executed within a controlled cleanroom environment to ensure the superior quality of the fabricated devices.

4.2 Characterization techniques

The samples used in this study are prepared using mechanical exfoliation and CVD processes. The prepared samples are first examined using several material characterization methods to ensure the high-quality and analyze the optical properties of the materials. Additionally, the characterization processes also usher new application possibilities for the samples.

4.2.1 Optical spectroscopies

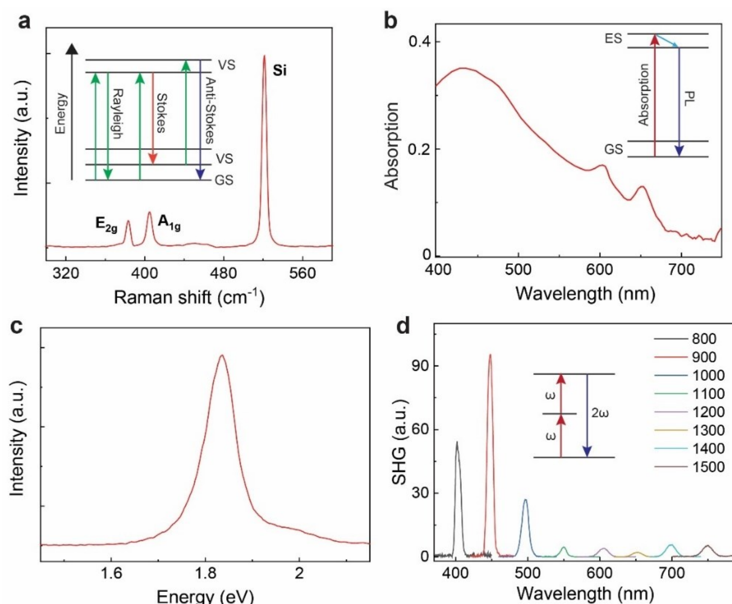

Figure 4.5. The optical spectroscopies for characterizing 2D materials. **(a)** Typical Raman modes from a few-layer MoS_2 sample. The E_{2g} and A_{1g} are the characteristic Raman modes of MoS_2 and the peak at ~521 cm^{-1} belongs to Si substrate. Inset shows Rayleigh, Stokes, and anti-Stokes scattering processes when light interacts with the material. VS and GS represent virtual and ground states, respectively. **(b)** Optical absorption spectrum of a monolayer MoS_2. The electron transition from GS to excited state (ES) by absorption process, and transition from the ES to GS while releasing energy in the form of PL, is shown in the inset. **(c)** PL response from a monolayer MoS_2. **(d)** SHG signals from a MoS_2 sample using 800-1500 nm excitation wavelengths. The inset presents a SHG process schematic, in which a new photon of frequency 2ω is generated from two incident photos with frequency ω. **(a)** and **(c)** are reproduced from **Publication I**, and **(d)** is reproduced from **Publication II**.

Optical spectroscopies play an important role in unraveling the unique properties of 2D materials. Raman spectroscopy involves shining laser light onto a sample and analyzing the scattered light. In elastic scattering or Rayleigh scattering, the scattered photons have the same energy as the incident photons. The majority of photons in this process experience elastic scattering. However, a small number of scattered photons show energy shifts relative to the incident photons, leading to Stokes and anti-Stokes scattering, as illustrated in the inset of Figure 4.5a. These types of scattering are known as inelastic scattering. These inelastic scatterings form Raman signals, which are distinct for each material[124]. Raman response from a 2D material provides insights into the

vibrational and lattice characteristics of the material, which can be used to extract information about its crystal structure, defects, doping, and strain. For instance, Raman spectroscopy can be used to distinguish different polymorphs of TMDCs and estimate the thickness of the material from the difference in the peak positions of Raman shifts. The scattering processes resulted from a light interacting with a material and the Raman modes (E_{2g} and A_{1g}) of MoS_2 upon irradiation of 532 nm laser are shown in Figure 4.5a.

Another useful tool is absorption spectroscopy, which measures the material's absorption of light at different wavelengths. This approach helps in determining the energy bandgap and the composite of 2D materials, providing information on their electronic structure and properties. For example, absorption spectroscopy can measure the energy bandgap of graphene oxide, assisting in understanding its optical properties and potential applications.[125], [126] Figure 4.5b shows the absorption spectrum of a monolayer MoS_2.

Photoluminescence (PL) spectroscopy involves exciting a material with light and analyzing the emitted light. In this process, electrons in the material absorb energy from incident light and then jump to higher energy states. When the electrons revert to their lower energy states, they emit the excess energy in the form of photons, producing a distinctive luminescent signal from the material. This approach is very beneficial for semiconducting 2D materials like TMDCs, as it helps in determining bandgap energy and emission properties. Researchers can acquire a better understanding of the electronic transitions within these materials and their excitonic characteristics by investigating the PL spectra.[127] A typical PL response from a monolayer MoS_2 is presented in Figure 4.5c.

Additionally, harmonic generation is a fundamental optical phenomenon that involves the interaction of light with a nonlinear medium, resulting in the generation of new frequencies that are integer multiples of the incident light frequency. Three prominent types of harmonic generation are the second harmonic generation (SHG), the third harmonic generation (THG), and the high harmonic generation (HHG). SHG produces photons with twice the energy of the incident photons, whereas THG generates photons with triple the energy. HHG occurs in intense laser fields, emitting high-energy photons that provide insights into ultrafast lasing processes. If an electric field (E) is applied to a material, the polarization (P) can be written as [128]:

$$P(t) = \varepsilon_0 \left(\chi^{(1)} E(t) + \chi^{(2)} E(t)E(t) + \chi^{(3)} E(t)E(t)E(t) + \cdots \chi^{(n)} E^n(t) \right) \quad (4.1)$$

where ε_0 is the vacuum permittivity and the coefficients $\chi^{(n)}$ are the nth-order susceptibilities of the material.

These phenomena are important for studying material properties and ultrafast dynamics. SHG, THG, and HHG signals can be generated from 2D materials, opening new possibilities for these materials in advancing attosecond physics and nanophotonics. The SHG signals generated from a MoS_2 sample using 800-1500 nm laser wavelengths and a schematic of SHG signals are presented in Figure 4.5d.

In this study, Raman and PL spectra are obtained at room temperature utilizing a micro-Raman setup (WITec alpha300 RA+) in a back-scattering configuration. A 532 nm laser, focused to a spot size smaller than 1 μm through a ×100 objective with 0.9 NA, serves as the excitation source. To prevent potential sample damage induced by the laser, a low laser power (<500 μW) is employed during the measurements.

An ultrafast femtosecond laser (Spectra-Physics, TOPAS) is employed to extract SHG, THG, and HHG. The laser has a pulse width of 230 fs and a repetition rate of 2 kHz. Focusing on the sample is achieved using a ×40 objective lens with NA of 0.75, resulting in a spot size of approximately 2.5 μm. A photomultiplier tube (PMT) with a monochromator (Andor 328i) detects the nonlinear responses from the samples in reflection mode. The SHG mapping is performed with a custom-built multiphoton system. The repetition rate is 84.49 MHz for the ultrafast laser at 800nm. The beam is focused on the sample using a ×40 objective lens with NA of 0.75. The SHG signals are detected by the PMT and are subsequently filtered to eliminate the seed laser.

4.2.2 Electron microscopies

Scanning electron microscopy (SEM) and transmission electron microscopy (TEM) are advanced imaging techniques that allow one to closely examine the morphology, structure, and composition of materials at the nanoscale.

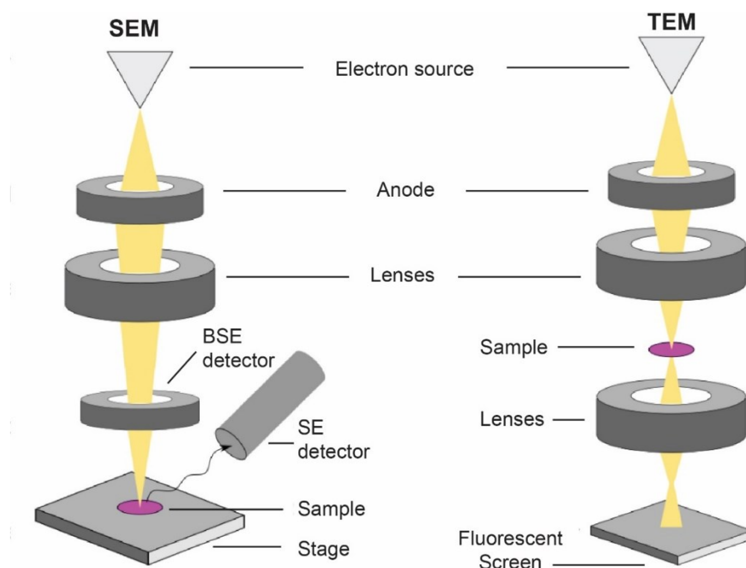

Figure 4.6. Schematic of the basic components of SEM (left panel) and TEM system (right panel)[129].

SEM involves scanning a focused electron beam over a sample's surface while collecting and analyzing the secondary and back-scattered electrons using the detectors to form images. The generated images offer high-resolution topographical data that enables researchers to see the sample's surface characteristics, textures, and three-dimensional shapes. SEM is particularly useful for

examining the surface properties of materials, examining the size and distribution of particles, and investigating a variety of materials, including solid surfaces, biological specimens, and nanomaterials. Figure 4.6 shows the basic components of an SEM system on the left panel.

In contrast, TEM takes imaging to an even finer level by allowing researchers to observe samples in cross-sections and obtain atomic-scale information. Detailed images of the atomic lattice can be achieved using high-resolution transmission electron microscopy (HR-TEM). This allows researchers to view individual atoms, crystal defects, and nanostructures. Additionally, with the electron diffraction technique in TEM, it is possible to determine the arrangement of atoms within a sample and gain important knowledge about the crystallographic information of materials. The basic components of a TEM system are presented on the right panel of Figure 4.6.

SEM and TEM techniques play pivotal roles in 2D science to investigate the microstructure and characteristics of materials and contribute to the advancement of various fields such as nanotechnology, photonics, and materials engineering.

In this study, SEM images are taken using a Zeiss Supra 40, operated at 3–8 kV. Most of the SEM images are acquired using a 45° tilted stage for better perspectives. For collecting HR-TEM images, a double aberration-corrected field emission gun microscope (JEOL 2200FS) is used, with 200 kV of electron acceleration voltage.

4.2.3 X-ray photoelectron spectroscopy

X-ray photoelectron spectroscopy (XPS) is an effective surface-sensitive approach to analyze the elemental composition, chemical states, and electronic structure of materials. In this process, when X-ray photons are focused onto a sample's surface, photoelectrons are ejected from the sample's outermost atomic layers. The binding energies of elements and their chemical environments are obtained by measuring the kinetic energy and quantity of photoelectrons released during the process. This information helps to identify oxidation states, chemical bonding, and impurities on the surface of the material. Additionally, the accuracy of the method is further improved by high-resolution XPS, which provides more details about chemical bonding and enables researchers to distinguish minute differences between chemical states. XPS has demonstrated its value across several scientific disciplines, including surface chemistry, catalysis, and materials research, providing insights into surface properties that influence a material's behavior and functionality. A typical XPS system with basic components is presented in Figure 4.7.

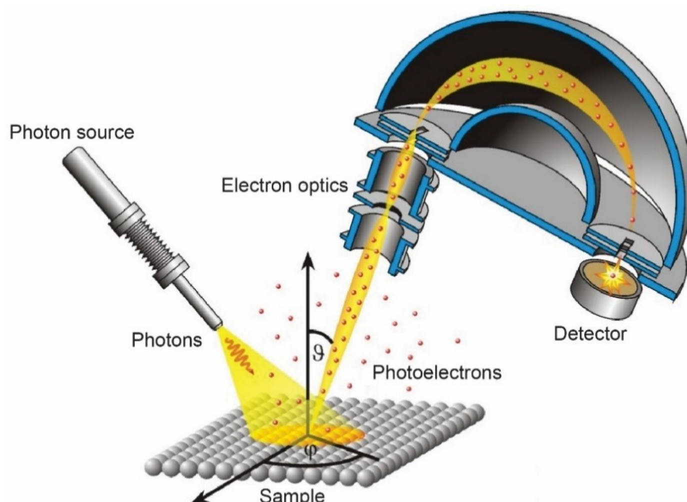

Figure 4.7. Schematic of a typical XPS measurement system[130].

In this study, XPS is used to study the chemical composition and chemical bonding states of the materials. The procedure is conducted using the Kratos Axis Ultra system, equipped with a monochromatic Al Kα (1486.96 eV) source. The analysis area for the wide scans is 300 × 700 μm. High-resolution scans are carried out with a 20 eV pass energy and a 0.1 eV energy step. To ensure accuracy, all spectra are calibrated against the C1s peak at 284.6 eV.

4.2.4 Atomic force microscopy

Atomic Force Microscopy (AFM) is a versatile imaging technology that enables scientists to characterize and manipulate materials at the nanoscale with very high resolution. Schematic of a typical AFM system is presented in Figure 4.8a. Unlike traditional optical microscopes that utilize light, AFM utilizes a sharp probe tip, typically composed of silicon or silicon nitride, for scanning the surface of a sample placed on a piezo scanner stage that can move in the XYZ directions. The tip scans the surface in contact, non-contact, or tapping mode. A laser beam is directed onto the tip to monitor its deflection as it interacts with the surface. A photodetector collects the laser beam reflected from the back of the tip and produces a precise topographic map of the material's surface features by assessing the forces between the tip and the sample via a feedback control system and a computer. This enables researchers to examine various physical and chemical properties, including roughness, elasticity, adhesion, and even electrical conductivity.

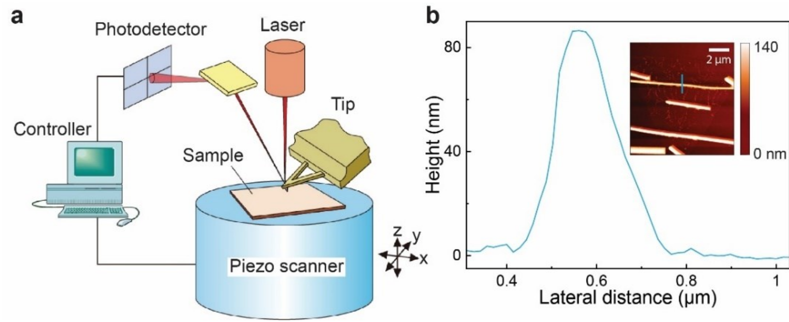

Figure 4.8. AFM measurement of a sample. **(a)** Schematic of an AFM system with basic components[131]. **(b)** Height profile of a MoS_2/NW_{AlGaAs} heterostructure. **(b)** is reproduced from **Publication I**.

In this study, AFM Dimension Icon is used for measuring the thickness and surface roughness of materials, and depth of profiles. The analysis area is around 1 - 10 μm with a scanning frequency of 0.5 Hz. Figure 4.8b shows the height profile measurement of a MoS_2/NW_{AlGaAs} heterostructure with an AFM-scanned image in the inset.

4.2.5 Electrical measurements

2D TMDC-based FETs hold great promise for future nanoelectronics owing to their unique properties originating from their 2D nature. The versatile band structure of these semiconducting materials and their heterostructures create a new platform for novel electronic and optoelectronic devices. The precise electrical characterization procedures are very crucial to effectively integrate these 2D FETs into practical electronic circuits.

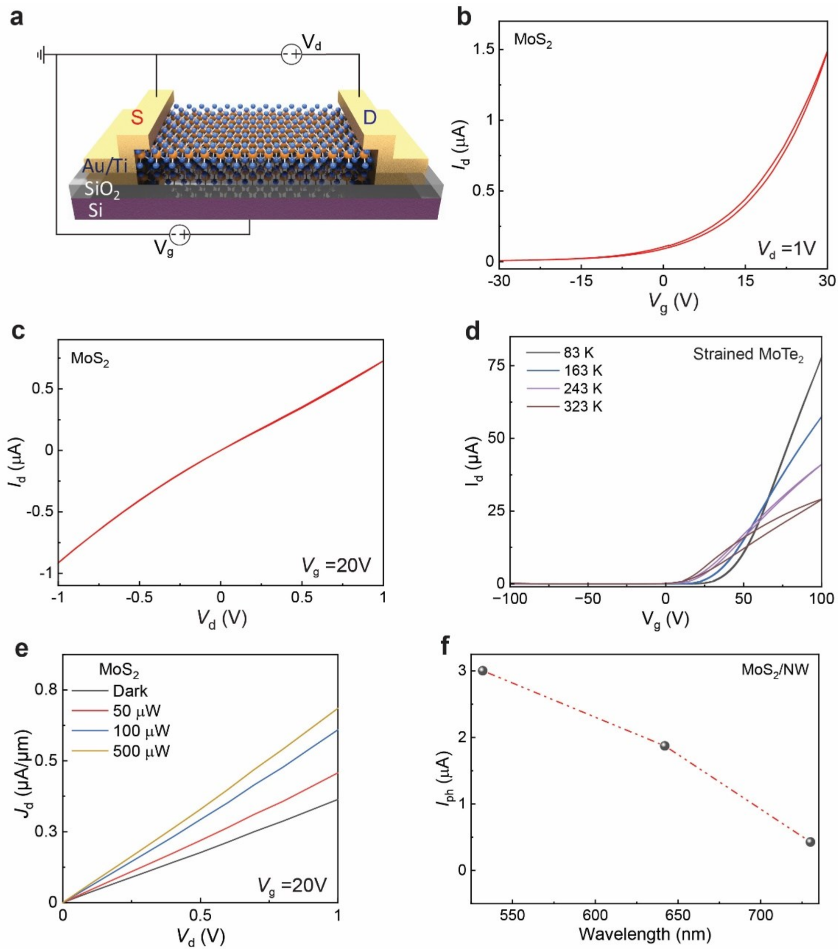

Figure 4.9. Electrical and photocurrent measurements of TMDC-based FETs. **(a)** Schematic of a typical TMDC-based FET. **(b)** Transfer curve, **(c)** output curve of a few layer MoS_2 device. **(d)** Temperature-dependent transfer characteristics of a strained $MoTe_2$ FET. **(e)** Current density of MoS_2 device under 532 nm laser at various power levels. **(f)** Photocurrent from MoS_2/NW_{AlGaAs} device at different laser wavelengths. **(a)**, **(e)** and **(f)** are reproduced from **Publication I**, and **(d)** is reproduced from **Publication IV.**

The research on 2D FETs mostly focuses on achieving high conductivity, high mobility, high on-off ratio (I_{ON}/I_{OFF}), and most importantly low power consumption. Consequently, electrical measurements of these FETs involve the characterization of their electronic properties and performance through various parameters such as conductivity, carrier density, threshold voltage (V_{th}), I_{ON}/I_{OFF}, mobility, etc. Most of these parameters can be extracted from the current-voltage characteristics (*I*-*V* curves). Figure 4.9a illustrates a schematic representation of a TMDC-based back-gate FET, in which highly doped Si, a thin layer of SiO_2, and Au/Ti pads are used as gate, dielectric, and source (S) and drain (D) electrodes of the device, respectively.

Two-point probe (2PP) and four-point probe (4PP) measurements are fundamental techniques for evaluating the resistivity and conductivity (reciprocal of resistivity) of TMDCs. The total channel resistance (R_{CH}) in a 2D FET is a

combination of the sheet resistance (R_{SH}), which characterizes the resistance of a unit area of the material, and the contact resistance (R_C) between the electrodes and the 2D channel, which can be written as $R_{CH} = R_{SH} + R_C$. In the 2PP setup, voltage and current are applied and measured through the same two terminals, resulting in a calculation of only the R_{SH}. However, due to the 2D nature of the channel, the impact of the contact material becomes more pronounced, potentially leading to higher contact resistance, which is disregarded in the 2PP configuration. The schematic of the 2D FET depicted in Figure 4.9a shows the 2PP configuration used for all electrical measurements in this study. The 4PP configuration addresses this concern by utilizing four distinct probes, thereby circumventing the influence of contact resistance and enabling precise determination of both channel resistivity and conductivity.[132]

As the FET comprises three terminals: source, drain, and gate, the voltage is applied individually through the source-drain terminal (V_d) and the gate terminal (V_g) to control the drain current (I_d) within the device. Based on the relationship between I_d and either V_d or V_g, the current-voltage characteristics are classified into two types: output characteristics (I_d-V_d curve) and transfer characteristics (I_d-V_g curve). Output characteristics are obtained by sweeping V_d while maintaining a constant V_g to measure I_d, while transfer characteristics involve sweeping V_g at a constant V_d to determine I_d. These characteristic curves play an important role in identifying the polarity of the TMDC-based FET. Figures 4.9b and c show the transfer and output characteristics of a few-layer MoS_2 device. Remarkably, this device exhibits n-type polarity, as illustrated in Figure 4.9b, where I_d increases with increasing positive gate voltages (V_g).

The V_{th} is a pivotal parameter in FET analysis. It represents the V_g at which the device transitions from the off-state to the on-state. It signifies the minimum voltage required to initiate current flow between the source and drain terminals. A lower V_{th} enhances the device's efficiency. The I_{ON}/I_{OFF} is determined by the ratio of I_d in the on-state (I_{ON}) to the off-state (I_{OFF}), indicating the FET's switching capability. This is important for digital logic circuits and low-power electronics. Additionally, mobility (μ) is also a crucial parameter for 2D FET. It can be calculated as

$$\mu = \frac{L}{W}\left(\frac{1}{C_{oxA}} + \frac{1}{C_{oxB}}\right)\frac{1}{V_d}\frac{dI_d}{dV_g}, \tag{4.1}$$

where L and W are the length and width of the 2D channel, and C_{oxA} and C_{oxB} are capacitances of A and B oxides. Mobility reflects charge carrier speed under an electric field, providing insights into device speed and conductivity.

Furthermore, the Schottky barrier height (SBH) at the metal-semiconductor interface refers to the energy barrier for injecting charge carriers, and hysteresis, indicating the variation in the behavior of the device in the forward and reverse sweep due to charge trapping and de-trapping, are important parameters in understanding the performance of 2D FETs. Temperature-dependent measurements of the FETs offer valuable insights into these effects. For instance, variations in SBH with temperature can reveal the charge transport mechanisms and interface properties. Similarly, hysteresis behavior can be better

comprehended by examining its temperature dependence, revealing the role of charge trapping and de-trapping processes. Figure 4.9d shows the transfer curves of a strained $MoTe_2$ device at various temperatures. As the temperature increases from 83 K to 323 K, the hysteresis window becomes wider. This suggests that there are more available states for charge trapping and de-trapping within the device.

4.2.6 Photocurrent measurements

Photocurrent (I_{Ph}) measurements are important in determining the optoelectronic characteristics of 2D TMDC-based FETs. These measurements provide insights into the capacity of the FET to transform incoming light into electric current. The charge carriers are excited when photons are absorbed by the material and cause a current flow between the FET's source and drain terminals. The I_{Ph} in a device is the difference in the I_d generated due to the illumination of light (I_{light}) and dark current (I_{dark}). It can be expressed as, $I_{Ph} = I_{light} - I_{dark}$. Figures 4.9e and f demonstrate the current density of a MoS_2 device under the irradiation of a 532 nm laser at varying power levels and the I_{Ph} response of MoS_2/NW_{AlGaAs} heterostructure at different wavelengths, respectively.

Two main parameters define 2D FET's performance as an optoelectronic device. Responsivity (R) is usually the first parameter derived from I_{Ph} measurements that indicates the device's light sensitivity. It is defined as the I_{Ph} produced per incident optical power unit. A higher R indicates a stronger sensitivity to light and, as a result, a more effective conversion of photons into electrical current. R is a key factor in evaluating the performance of photodetectors and photovoltaic devices.

Detectivity is another pivotal parameter to assess the ability of the device to detect weak lights. It calculates the minimum detectable optical power while considering both the device's R and noise. A higher detectivity means superior low-light performance, making the device appropriate for use in sensors and imaging device applications.

The following expressions can be used to calculate R and specific detectivity (D^*) for a photodetector.

$$R = \frac{I_{ph}}{P_{in}}, \quad (4.2)$$

$$D^* = \frac{RA^{1/2}}{(2eI_{dark})^{1/2}}, \quad (4.3)$$

where P_{in}, A, and e are denoted as irradiated laser power, illuminated area, and the electron charge, respectively.

5. 2D-1D Heterostructures for Photonics

In this thesis, two types of 2D-1D mixed-dimensional heterostructures are studied for photonic and optoelectronic applications. Firstly, MoS_2 is transferred onto NW_{AlGaAs} with a high refractive index to form MoS_2/NW_{AlGaAs} heterostructures. These heterostructures facilitate enhanced optical responses from MoS_2. Secondly, NW_{InP} are epitaxially grown directly on CVD-grown MoS_2, creating NW_{InP}/MoS_2 heterostructures. These heterostructures exhibit strong linear and nonlinear optical behaviors. A comprehensive analysis of these heterostructures is provided in this chapter.

5.1 Enhancement of optical properties

The light-matter interactions and symmetry of monolayer MoS_2 can be engineered by utilizing NW_{AlGaAs} to create mixed-dimensional heterostructures. For this purpose, NW_{AlGaAs} are transferred onto SiO_2/Si substrate, and subsequently, CVD-grown or mechanically exfoliated monolayers MoS_2 are transferred on nanowires. An optical image of the MoS_2/NW_{AlGaAs} heterostructure is shown in Figure 5.1a. The characteristic Raman spectra of MoS_2 monolayer, NW_{AlGaAs}, and MoS_2/NW_{AlGaAs} using 532 nm (~ 2.33 eV) laser excitation are presented in Figure 5.1b. The in-plane E^1_{2g} (~ 385.50 cm^{-1}) and out-of-plane A_{1g} (~ 405 cm^{-1}) of MoS_2, and the strong longitudinal optical mode (LO) of NW_{AlGaAs} at ~260 cm^{-1} are observed. These modes' positions match with the previous reports[133]–[135]. The Si substrate Raman peak is also observed at ~521 cm^{-1}.

In this study, the light-matter interaction in MoS_2/NW_{AlGaAs} heterostructures is examined by comparing the linear optical responses of bare MoS_2 and the heterostructure using 532 nm laser excitation. Figure 5.1c reveals identical Raman modes of MoS_2 from the MoS_2/NW_{AlGaAs} heterostructure and monolayer MoS_2 that confirm the intact quality of the transferred MoS_2 on the NW_{AlGaAs}. Interestingly, the Raman intensity of MoS_2 from the MoS_2/NW_{AlGaAs} heterostructure is ~3 times higher than that of bare MoS_2. A slight peak shift of about -0.6 cm^{-1} is observed for both modes in the Raman spectrum of the MoS_2/NW_{AlGaAs} structure compared to bare MoS_2 which indicates minor strain and doping effects[136]–[139]. The induced strain in the MoS_2 due to the NW_{AlGaAs} is estimated to be ~ 0.3 %, which is negligible considering the reported strain-induced mode shifts[140].

The room temperature PL spectra in Figure 5.1d display a ~ 9-fold stronger emission from the MoS_2/NW_{AlGaAs} heterostructure compared to bare MoS_2. A slight blue shift of ~ 25 meV of the MoS_2 A-exciton peak in the heterostructure

is noticed which could be attributed to the reduced exciton binding energy due to increased Coulomb screening of MoS_2 induced by the MoS_2/NW_{AlGaAs}. The observed blue shift in the PL also suggests that strain does not contribute to the enhancement of light-matter interactions in the heterostructure, as uniaxial tensile strain usually leads to a red shift in the PL response[140], [141].

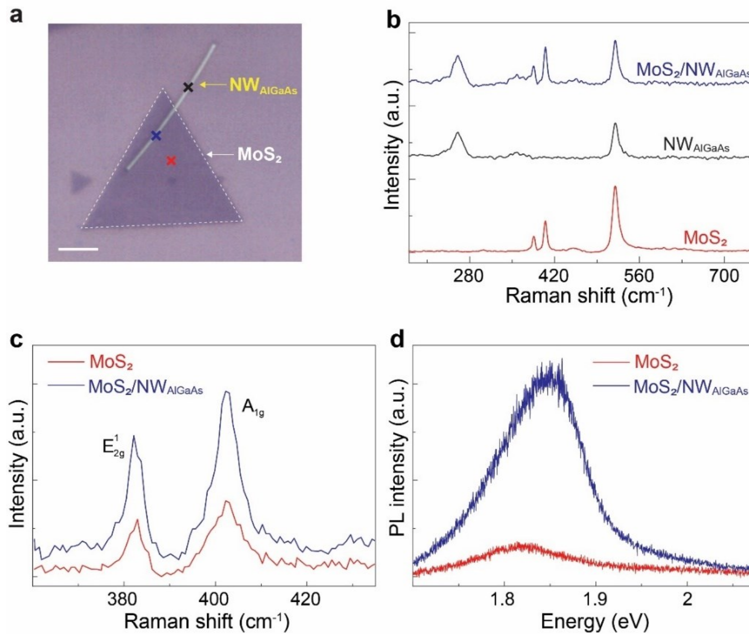

Figure 5.1. MoS_2/NW_{AlGaAs} heterostructure for enhancing optical response. **(a)** Optical image of the heterostructure. Scale bar: 5 μm. **(b)** Room temperature Raman signals from each material and heterostructures. The spectra of NW_{AlGaAs}, MoS_2, and MoS_2/NW_{AlGaAs} heterostructure are collected from the black, red, and blue cross points in **(a)**, respectively. Comparison of the room-temperature **(c)** Raman and **(d)** PL spectra of MoS_2 and MoS_2/NW_{AlGaAs}. Adapted from **Publication I.**

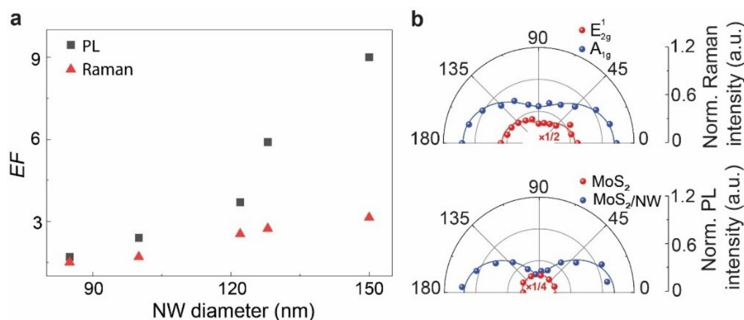

Figure 5.2. Anisotropy in Raman and PL spectra in the heterostructures. **(a)** NW_{AlGaAs} diameter-dependent Raman and PL *EF* in the heterostructure. **(b)** Normalized intensity variations of the E^1_{2g} and A_{1g} Raman modes in MoS_2/NW_{AlGaAs} heterostructure (top panel). Change in PL intensity in bare MoS_2 and MoS_2/NW_{AlGaAs} at various polarization angles of the illuminated light (bottom panel). The polarization angle θ is formed by the NW_{AlGaAs} long axis and the angle of polarization detection for both cases. Adapted from **Publication I.**

The enhancement factor (*EF*) for Raman and PL signals, characterized by the intensity ratio in MoS_2/NW_{AlGaAs} and bare MoS_2, varies with different diameters of nanowires. In this study, nanowires with diameters ranging from 80 to 150 nm are utilized to investigate the *EF* variation. Generally, *EF* increases as the NW_{AlGaAs} diameter increases, as illustrated in Figure 5.2a. This phenomenon could be attributed to the larger diameter of the NW_{AlGaAs}, resulting in a greater interfacial area in the heterostructures. The highest *EF* of ~ 3 and ~ 9 is recorded with nanowires having ~ 150 nm diameter for Raman and PL responses, respectively.

Additionally, the top panel of Figure 5.2b illustrates variations in Raman intensity in the MoS_2/NW_{AlGaAs} heterostructure based on the polarization angle of the incident light using a polar diagram. The maximum and minimum intensities of MoS_2 Raman modes are collected when the linearly polarized pump light's polarization angle aligns parallelly ($\theta = 0\ ^\circ$) and perpendicularly ($\theta = 90^\circ$) to the nanowire's long axis, respectively. The degree of anisotropies for E^1_{2g} and A_{1g} modes are calculated as 34 % and 36 %, respectively, using this expression: $(I_{max} - I_{min})/(I_{max}+I_{min})$[123]. Figure 5.2b depicts a polar plot for comparing polarization-dependent PL responses of bare MoS_2 and MoS_2/NW_{AlGaAs} heterostructure. PL from bare MoS_2 shows no polarization angle dependency. In contrast, the heterostructure exhibits a highly anisotropic PL response. The PL intensity is maximum when the excitation polarization aligns parallel to the NW_{AlGaAs} axis, whereas the minimum intensity results with the perpendicular alignment. The MoS_2 PL from the heterostructure exhibits a 60% degree of anisotropy. This strong anisotropy is attributed to the breaking of C_3 rotational symmetry of the MoS_2 monolayer due to the reduction of effective dimensionality from 2D to 1D within the heterostructure region[142].

5.1.1 Charge transfer and nanowire's confined field

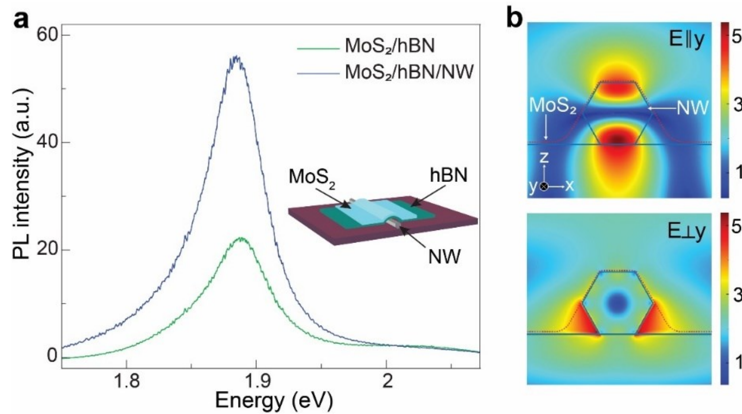

Figure 5.3. Investigation of the reasons behind the enhanced optical properties of $MoS_2/\ NW_{AlGaAs}$ heterostructure. (a) Comparison of the PL spectra from MoS_2/hBN and $MoS_2/hBN/NW_{AlGaAs}$ heterostructures for analyzing the possibility of charge transfer. The inset shows a schematic of the hBN-inserted heterostructure. (b) Numerical simulations showing EM field distribution around $MoS_2/\ NW_{AlGaAs}$ heterostructure with excitation polarization angle aligned parallel (top panel) and perpendicular (bottom panel) to the NW_{AlGaAs} long axis (y-axis). Adapted from **Publication I.**

The enhanced PL from the MoS_2/NW_{AlGaAs} heterostructures can arise due to two factors, charge transfer[143]–[145] and optical confinement in NW_{AlGaAs}. With an Al composition of about 30 % in the NW_{AlGaAs}, MoS_2, and NW_{AlGaAs} energy diagrams suggest a type-II band alignment at the heterostructure region. This alignment is expected to result in quenched MoS_2 PL emission[146], however, an increase in the PL is observed. To rule out the possibility of charge transfer, ~ 11 nm of insulating hBN layer is inserted between MoS_2 and NW[147]. Interestingly, the heterostructure still exhibits enhanced PL response upon 532 nm laser illumination. The PL from the $MoS_2/hBN/NW_{AlGaAs}$ heterostructure is ~ 3 times stronger than the MoS_2/hBN structure, as shown in Figure 5.3a. This confirms that the charge transfer has no contribution to MoS_2 PL enhancement.

Numerical simulation based on finite element modeling is performed to find the source of the enhanced optical response in the MoS_2/NW_{AlGaAs} heterostructure. This simulation takes into account several parameters, including a monolayer of MoS_2 and a 100 nm diameter NW_{AlGaAs} with refractive indices (n) of 3[148] and 3.5[149], respectively, a SiO_2/Si substrate with a 285 nm thick SiO_2 layer (n = 1.45), and excitation at a wavelength of 532 nm with linear polarization. The simulation result is shown in Figure 5.3b. It reveals that the electromagnetic field (EM) is strongly confined in the NW_{AlGaAs} due to its high aspect ratio and relatively large refractive index contrast compared to the surrounding medium. The confinement is more concentrated at the top and bottom of the nanowire when the excitation light is parallel to the nanowire axis. However, the EM confinement is more localized only at the bottom of the nanowire in the perpendicular configuration. The strong field confinement at the top of the NW_{AlGaAs} enhances the light-matter interactions in MoS_2, resulting in a higher rate of exciton excitation in the heterostructure region compared to bare MoS_2. These results are in strong accordance with experimentally observed enhanced optical response from the heterostructures.

5.2 Enhancement of optoelectronic properties

Photodetectors with enhanced performance can be fabricated by harnessing the improved optical response of MoS_2/NW_{AlGaAs} heterostructure. The optical field confinement in NW_{AlGaAs} also impacts the R and D^* of MoS_2/NW_{AlGaAs} -based phototransistors. Intriguingly, these devices can also produce anisotropic photocurrents which is a new feature to their functionality. Figure 5.4a illustrates the calculated I_{Ph} values of MoS_2 and MoS_2/NW_{AlGaAs} heterostructure at 50–500 µW of 532 nm laser illumination. I_{ph} curves get saturated in both phototransistor types. In contrast to the bare MoS_2 photodetector, notable I_{ph} enhancements of ~ 5 and ~ 8 times are observed from the MoS_2/NW_{AlGaAs} device at laser powers of 50 µW and 500 µW, respectively. This enhancement can be attributed to the strong EM confinement at the NW_{AlGaAs} top, which reinforces the applied electric field in the MoS_2 channel. This creates more photo-generated carriers and transports them towards the electrodes.

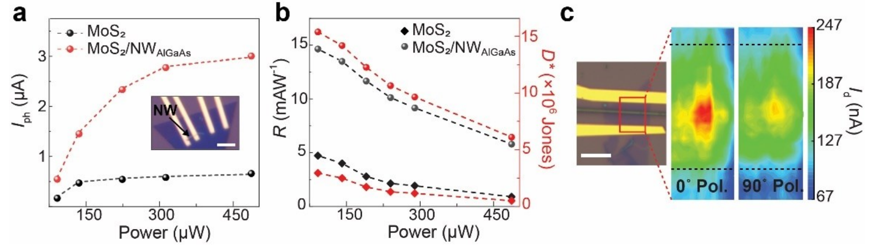

Figure 5.4. Improved performance and anisotropy in a mixed-dimensional MoS_2/NW_{AlGaAs} photodetector. **(a)** I_{Ph} from MoS_2 and MoS_2/NW_{AlGaAs} based devices under 532 nm laser at different powers. The inset shows the optical image of the sample. Scale bar: 2 μm. **(b)** Evaluating the *R* and *D** of the photodetectors for the incident laser power variation. **(c)** Optical image of the device used for the analysis of anisotropic photoresponse from MoS_2/NW_{AlGaAs} heterostructure (left panel). The I_{Ph} maps with 0° and 90° excitation polarizations are taken from the red box area of the optical image. The inner boundaries of the electrodes are shown in black dashed lines in the maps. Adapted from **Publication I.**

The *R* and *D** of the devices are calculated using Equations 4.2 and 4.3, respectively. A comparison between the *R* and *D** values of MoS_2 and MoS_2/NW_{AlGaAs} devices is depicted in Figure 5.4b, which also highlights the enhanced performance of the MoS_2/NW_{AlGaAs} device. At a laser power of 100 μW, the MoS_2/NW_{AlGaAs} device exhibits ~ 3 and ~ 5 times improvements in *R* and *D** values, respectively, compared to the MoS_2 device. Interestingly, the heterostructure-based devices show anisotropic photocurrents when polarized light is illuminated in parallel (0°) and perpendicular (90°) to the NW's long axis, similar to the optical responses presented above. This phenomenon is also attributed to the rotational symmetry breaking of MoS_2 by the NW. Figure 5.4c shows an optical image (left panel) and the anisotropic photocurrents of the heterostructure (right panel).

5.3 Nonlinear optics in epitaxially-grown heterostructures

NW_{InP} are promising for their applications in solar cells[73], light emitting diodes[150], photodetectors[151], and lasers[152] due to their direct bandgap, minimal surface recombination velocity, and exceptional optical quality[153]. In parallel, 2D MoS_2 possesses a direct bandgap in monolayers, substantial excitonic binding energy, strong luminescence, and high carrier mobility[7], [154]. By leveraging MoS_2 and InP's excellent nonlinear optical properties[155]–[157], it is possible to further enhance their potential for diverse photonic applications through the formation of mixed dimensional heterostructures.

5.3.1 Epitaxial growth of nanowires on TMDCs

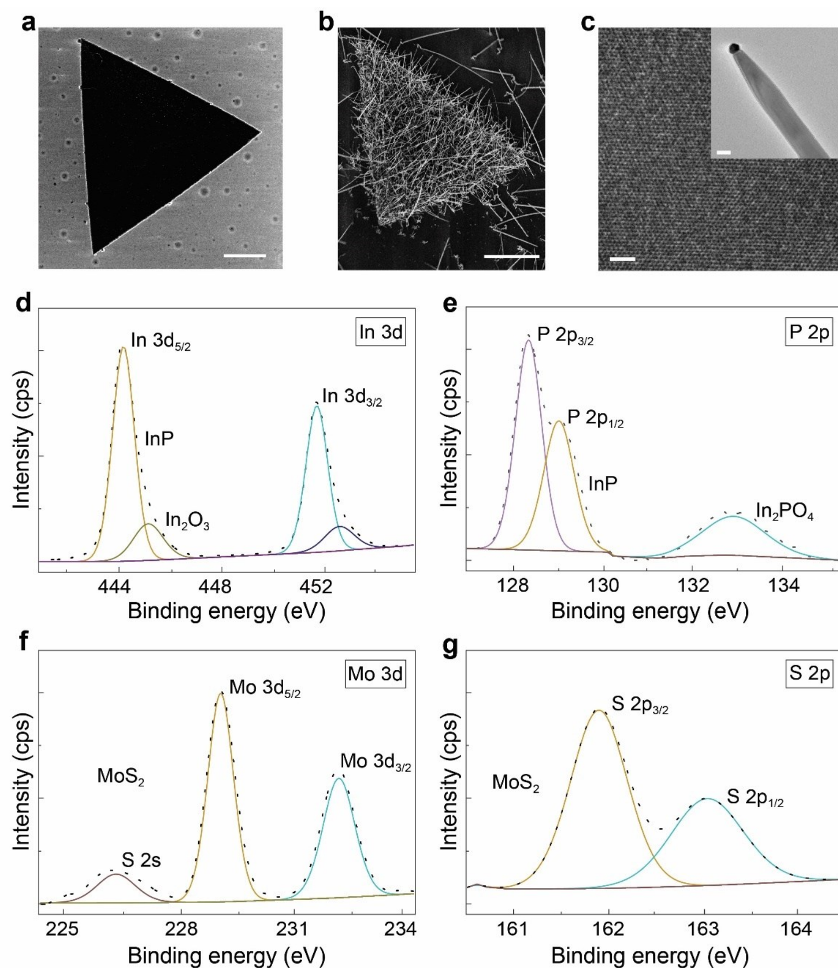

Figure 5.5. Growth of NW_{InP} on MoS_2. SEM images of **(a)** a CVD-grown MoS_2 crystal and **(b)** a VLS-grown NW_{InP}/MoS_2 heterostructure (45° tilted image). The scale bar for both images is 5 μm. **(c)** HR-TEM image of an as-grown NW_{InP}. Scale bar: 1 nm. The inset shows the TEM image of the corresponding nanowire. Scale bar: 50 nm. XPS spectra of **(d, e)** In-3*d* and P-2*p* core level regions and **(f, g)** Mo-3*d* and S-2*p* regions from NW_{InP}/MoS_2, respectively. Adapted from **Publication II.**

This study shows a simple and effective approach to form mixed-dimensional heterostructures by epitaxially growing NW_{InP} onto monolayer MoS_2 synthesized using CVD. The growth of high-quality vertical nanowires on MoS_2 is facilitated by the aid of Au nanoparticles as seeds at low temperatures that ensure the thermal and chemical stability of MoS_2.

The MoS_2 monolayers and few-layer flakes are grown using optimized parameters in the CVD process with 10-100 μm flake size. Figure 5.5a shows an SEM image of an as-grown MoS_2 crystal. In this study, nanowires are grown on MoS_2 using the bottom-up VLS growth method. VLS NW_{InP} growth generally relies on Au droplets in a liquid solution that gathers vapor-phase growth elements and initiates solid-crystal NW_{InP} nucleation. This Au-seeded approach offers precise control over NW_{InP} characteristics while minimizing the radial

growth[158]. The successful vertical NW_{InP} growth on MoS_2 relies on several factors such as the V/III precursor ratio, precursor flow rate, and growth temperature. Optimized parameters during growth lead to adatoms accumulating on the MoS_2 surface under Au seeds, initiating the nucleation of nanowires beneath the nanoparticles. High-density NW_{InP} growth depends on the sticking coefficient (s = number of adsorbed atoms/number of desorbed atoms) and the number of Au particles on the substrate. MoS_2 with a high sticking coefficient[30] and PLL treatment of Au nanoparticles ensure the presence of sufficient seeds on MoS_2. Ostwald ripening of the seeds is prevented since the seeds are mounted via MoS_2 fixation which also encourages self-supported, dense, and vertical NW_{InP} growth. Figure 5.5b presents a 45 ° tilted SEM image of an epitaxially-grown NW_{InP}/MoS_2 heterostructure. These nanowires exhibit an average height of approximately 8 μm and a notably high yield of vertically aligned nanowires (~ 1 μm^{-2}). The HRTEM image showing the atomic structure of the NW_{InP} is presented in Figure 5.5c while a TEM image of the NW_{InP} having an Au nanoparticle at the NW_{InP} tip is presented in the inset.

The growth of NW_{InP} on the surface of MoS_2 is challenging due to their lack of dangling bonds. The edges of MoS_2 provide the required dangling bonds for vdW epitaxial growth of in-plane and out-of-plane nanowires. Raising the temperature during any annealing process can introduce dangling bonds on the entire MoS_2 flake, encouraging nanowire growth on the surface but also leading to defects and oxidation of the flake[159]. This can degrade the intrinsic properties of MoS_2, initiate the growth of parasitic islands, and alter the phase and structure of the MoS_2. In this approach, NW_{InP} are grown on MoS_2 flakes at 430 °C to ensure MoS_2 stability while growing high-quality nanowires. To check the chemical stability of MoS_2 during NW_{InP} growth, Raman and PL measurements are conducted before and after the PLL treatment and annealing the samples at 430 °C for 300 s. The results do not show any change in the signals, confirming the chemical stability of MoS_2 during nanowire growth. The chemical and thermal stability of MoS_2 makes the material promising for nanowire-integrated high-performance photonic and optoelectronic devices. Moreover, MoS_2's lattice structure provides a favorable platform for vdW epitaxial growth because of its lattice parameter of 3.16 Å, which is compatible with the relatively larger lattice parameters of III-V NWs like InP (4.15 Å for the wurtzite phase and 5.86 Å for the zinc-blende phase). Due to its small mismatch with the wurtzite phase, MoS_2 is more favorable for the growth of NW_{InP} in the WZ configuration than in the zinc-blende configuration.

High-resolution XPS is employed to analyze the composition and quality of the NW_{InP}/MoS_2 samples. Figure 5.5d-g presents XPS spectra featuring emission peaks of In-3*d*, P-2*p*, Mo-3*d*, and S-2*p*. The In-3*d* core-level spectrum (Figure 5.5d) is deconvoluted into four peaks. Peaks at 444.3 eV (In-$3d_{5/2}$) and 451.8 eV (In-$3d_{3/2}$) correspond to InP, while peaks at 445.2 and 452.7 eV indicate In2O3. The P-2p spectrum (Figure 5.5e) exhibits InP peaks at 128.4 eV (P-$2p_{3/2}$) and 129.1 eV (P-$2p_{1/2}$), with an InPO4 peak at 133 eV. Both In-3*d* and P-2*p* spectra show higher relative intensities of InP which suggests favorable growth conditions for high-quality NW_{InP} growth on MoS_2 with less oxide formation. Additionally, characteristic MoS_2 emission peaks are also observed in the heterostructures. The S-2*s*, Mo-$3d_{5/2}$, and Mo-$3d_{3/2}$ peaks are at 226.3, 229.1, and 232.3 eV, as shown in Figure 5.5f. Similarly, Figure 5.5g shows an S-

$2p$ peak doublet at 161.9 and 163.1 eV, corresponding to S-$2p_{3/2}$ and S-$2p_{1/2}$ from the MoS_2 crystal. These results are matches with the prior reports[160], [161].

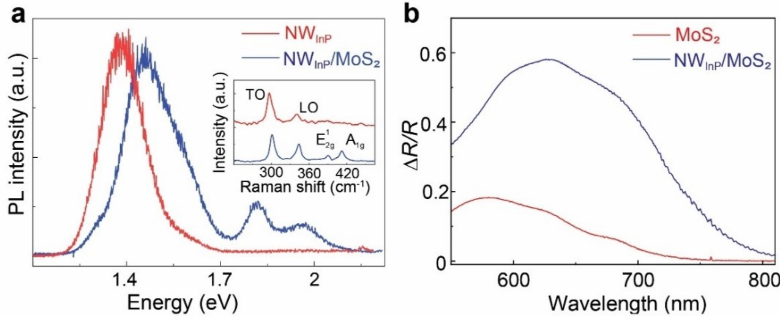

Figure 5.6. Optical response from the NW_{InP}/MoS_2 heterostructure. **(a)** Comparison of the PL responses from NW_{InP} and the heterostructure. The inset shows the Raman spectra of the samples. The TO and LO modes represent transverse and longitudinal optical phonon modes of NW_{InP}, respectively, whereas E^1_{2g} and A_{1g} are MoS_2 Raman modes. **(b)** Differential reflectivity difference between MoS_2 and NW_{InP}/MoS_2 samples in the visible range. Adapted from **Publication II.**

The optical response of the NW_{InP}/MoS_2 heterostructure is assessed by comparing its Raman and PL spectra with those of WZ NWs grown on Si (111), as shown in Figure 5.6a. Room temperature Raman spectra reveal the longitudinal optical (LO) and transverse optical (TO) phonon modes of nanowires grown on Si are at ~ 301 cm^{-1} and ~ 340 cm^{-1}, respectively. A similar pattern is observed for nanowires grown on MoS_2, however, there are ~ 2.2 cm^{-1} and ~ 3 cm^{-1} shifts in LO and TO modes, respectively. Additionally, the Raman spectrum of the NW_{InP}/MoS_2 heterostructure shows in-plane E^1_{2g} (~383.7 cm^{-1}) and out-of-plane A_{1g} (~ 403.1 cm^{-1}) vibrational modes of MoS_2. Correspondingly, the PL spectra of the heterostructure exhibit a ~80 meV blue-shift from the WZ phase of NW_{InP} on Si (~ 1.4 eV). The NW_{InP} grown on MoS_2 has a smaller effective diameter compared to those on a Si substrate due to surface depletion. Additionally, the diameter of NW_{InP} reduces at the top, resulting in a tapered shape of the nanowires after growth. This can lead to a quantum confinement effect. This reduction in NW_{InP} diameter on the MoS_2 surface and the quantum confinement effect at the top of the NW_{InP} may contribute to the PL blue shift [162], [163]. Furthermore, the heterostructure PL includes A-exciton and B-exciton signals of monolayer MoS_2. Raman and PL analyses confirm the intact quality of MoS_2 after NW_{InP} growth. Enhanced absorption in NW_{InP}/MoS_2 compared to bare MoS_2 across a broad-spectrum range (~ 550 nm to 800 nm) is also observed from differential reflectivity measurements, as shown in Figure 5.6b.

5.3.2 Generation of nonlinear optical responses

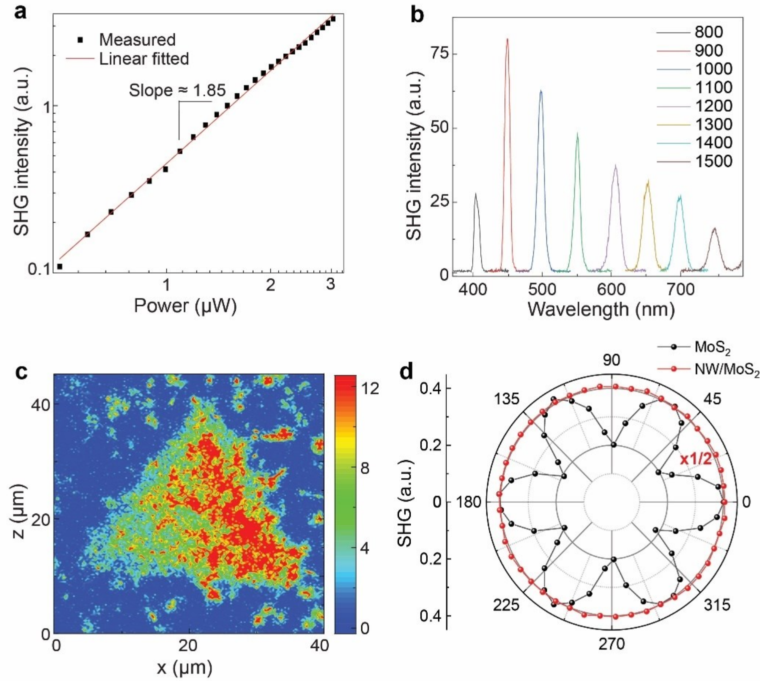

Figure 5.7. SHG from the NW_{InP}/MoS_2 heterostructures. **(a)** Power-dependent SHG intensities at various powers of 800 nm excitation. **(b)** SHG spectra under different wavelengths of excitation laser. **(c)** SHG mapping of a heterostructure using 800-nm laser. **(d)** Anisotropy in the SHG of MoS_2 and NW_{InP}/MoS_2 with 800 nm excitation. Adapted from **Publication II.**

The nonlinear optical behavior of the NW_{InP}/MoS_2 heterostructure is investigated. The second SHG, THG, and HHG signals are measured using an ultrafast femtosecond laser. Figure 5.7a shows power-dependent SHG intensity from the heterostructure with an 800 nm excitation wavelength. A slope of ~ 1.85 is observed from the linear fitting of the curve. SHG intensities vary across excitation wavelengths from 800 to 1500 nm, as shown in Figure 5.7b. The highest intensity was observed with 900 nm excitation due to resonance with InP emission energy. Figure 5.7c presents an SHG mapping that shows high-intensity SHG signals throughout the sample. Unlike bare MoS_2, which exhibits a six-fold SHG pattern, the heterostructure's SHG is polarization-independent due to NW_{InP} growth in random directions on MoS_2. However, the signal intensities are twice as strong as those of bare MoS_2, as depicted in Figure 5.7d.

Figure 5.8a presents power-dependent THG intensity in the heterostructure. It reveals third-order optical nonlinearity with a slope of ~ 2.81 at 1300 nm excitation. Strong and consistent THG signals are observed with 1200 to 1500 nm excitation wavelengths, as shown in Figure 5.8b. Intriguingly, the 4000 nm pump laser results in 5th and 7th-order harmonic generations at 800 nm and ~ 571 nm, respectively, as depicted in Figure 5.8c.

Both NW_{InP} and MoS_2 possess non-centrosymmetric crystal structures which generate strong lower-order (SHG and THG) signals and relatively weak HHG

signals from the heterostructures. However, NW_{InP} contribution is more significant than MoS_2 due to their higher density on MoS_2. Nevertheless, the non-uniform growth density of NW_{InP} on MoS_2 complicates quantifying each material's precise contribution to the nonlinear optical responses.

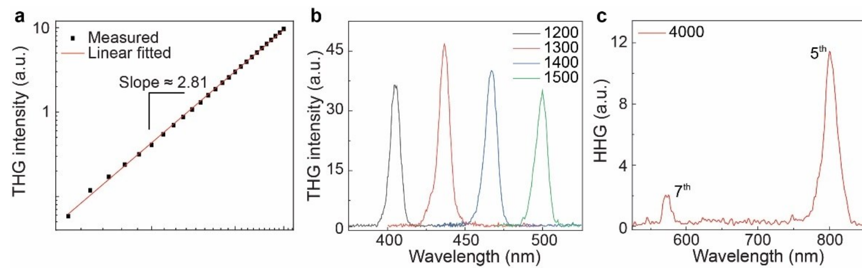

Figure 5.8. THG and HHG from the NW_{InP}/MoS_2 heterostructures. **(a)** Power-dependent THG intensities at 1300 nm pulse excitation. **(b)** THG spectra from the sample as a function of wavelengths. **(c)** 5th and 7th harmonic generation spectra from the sample using 4000 nm excitation. Adapted from **Publication II.**

6. Tuning Electronic Properties of TMDCs

This chapter focuses on tuning electronic the properties of TMDCs for fabricating high-performance devices through high-temperature treatment, the application of strain, and phase modulation by optical writing. Primarily, $MoTe_2$ is used as the study material due to its considerable potential in practical electronic circuitry. Detailed discussions of the techniques and their outcomes are presented systematically.

6.1 Effect of high-temperature treatment

6.1.1 Annealing and high-temperature impact

The polarity transition (n-type to p-type or vice-versa) in $MoTe_2$ devices can be influenced by modifying the metal-$MoTe_2$ contact through thermal treatment. However, thermally treated defective channels in $MoTe_2$ can also lead to polarity transitions, which are often overlooked when evaluating FET performance. In this study, two types of electro-thermal experiments are designed to investigate the impact of high temperatures on $MoTe_2$ FET with Au/Ni contacts. Initially, a multistep annealing process is explored where the temperature increases at a fixed rate and device response data is collected after each annealing cycle at room temperature. Figure 6.1a illustrates the step function plot of the annealing process. The device underwent gradual annealing, with temperatures increasing from 298 to 673 K in 25 K steps, and each annealing cycle lasting 30 minutes. The transfer curves collected at room temperature after each annealing cycle are presented in Figure 6.1b. The results reveal a peak in I_d at ~500 K. Temperature-dependent μ values are calculated from the transfer curves using Equation 4.1, with a 285 nm SiO_2 gate oxide (C_{ox}). Changes in the I_{ON}/I_{OFF} of the device as a function of annealing temperature are shown with the μ values in Figure 6.1c. The μ and I_{ON}/I_{OFF} values follow the same trend with respect to annealing temperature variations. To better understand the annealing effects, the changes in the curves can be divided into three regions. Region I (298 K to 398 K) shows minimal change in device performance, suggesting no significant impact of annealing temperatures on the device response. Region II (398 K to 498 K) demonstrates improved device performance due to the elimination of surface contaminations such as air absorbates and residues from the device fabrication processes during high-temperature annealing. The quality of the metal/$MoTe_2$ interface is also improved and contributed to the higher μ and I_{ON}/I_{OFF}. Region

III (up to 673 K) shows a decline in device performance due to high-temperature-induced structural changes and defect formations in the $MoTe_2$ channel. These results indicate that the optimal post-fabrication annealing temperature for $MoTe_2$ devices falls in the range of 450–525 K. This range enhances metal contact adhesion while ensuring device stability at high temperatures up to 673 K.

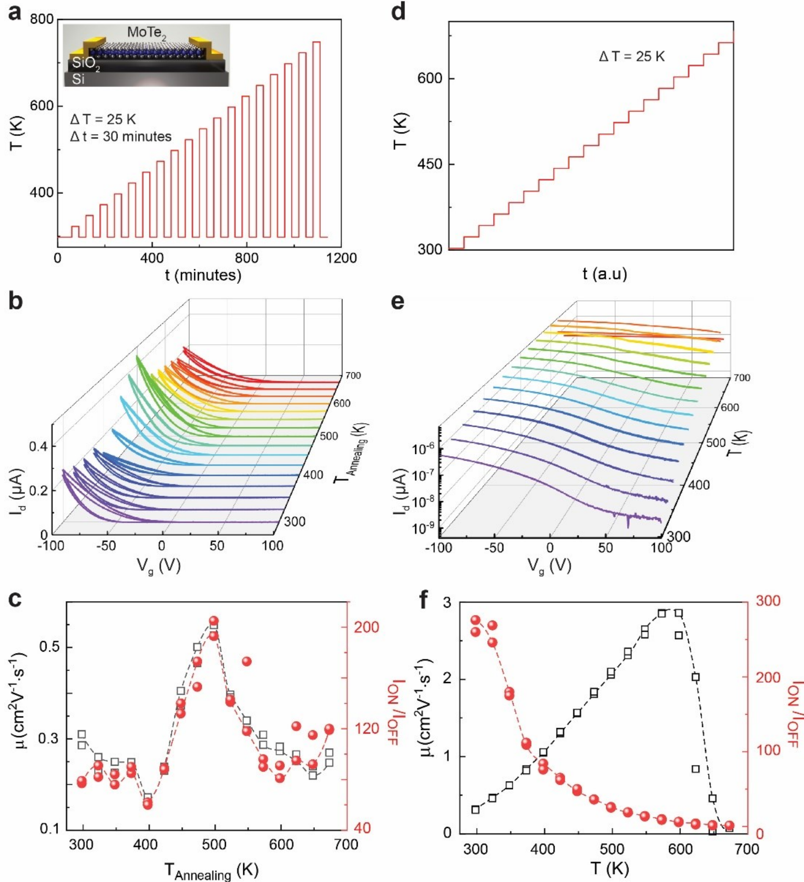

Figure 6.1. High-temperature effects on $MoTe_2$ FET electrical responses. **(a)** Illustration of the annealing process steps, with a temperature interval (ΔT) of 25 K and annealing time (Δt) of 30 minutes. All electrical measurements are conducted at room temperature after annealing. Inset presents the schematic of the $MoTe_2$ FET. **(b)** Transfer characteristics of a typical device at V_d = 1 V after annealing at varying temperatures. **(c)** Change in μ and I_{ON}/I_{OFF} of the devices after annealing. **(d)** Illustration of the gradual temperature increase during high-temperature measurements. Inset shows the work function values for nickel (Ni) and $MoTe_2$. **(e)** Transfer curves (at V_d = 1 V) for the FET at different temperatures. **(f)** Change in μ and I_{ON}/I_{OFF} of the devices after annealing different temperatures. Adapted from **Publication III.**

In the next experiment, electrical measurements are conducted while incrementally raising the stage temperature from room temperature to 673 K in 25 K intervals, as depicted in Figure 6.1d. The transfer characteristics at various temperatures are shown in Figure 6.1e. Both on-state and off-state currents in the device are increased simultaneously, leading to a reduction in the I_{ON}/I_{OFF} with temperature increase. Interestingly, under the same bias condition (V_d = 1 V),

the gating effect diminishes with elevating temperature. Therefore, $MoTe_2$ channel behaves like heavily p-doped at higher temperatures. Additionally, the off-state current shifted towards a more positive V_g that also indicates p-doping in the channel. The μ and I_{ON}/I_{OFF} are extracted from the transfer curves, as shown in Figure 6.1f. The μ value increased from 0.5 to 3 $cm^2\ V^{-1}\ s^{-1}$ to 598 K and then rapidly decreased towards 673 K due to material degradation resulting from repeated electrical and thermal stress. The decreasing gate dependency in the transfer curves, the μ–temperature trend, and the decrease in the I_{ON}/I_{OFF} with temperature suggest two possibilities: a temperature-induced phase modulation in $MoTe_2$ or other forms of transport mechanism in $MoTe_2$ channel at high temperatures.

6.1.2 Phase transition and surface oxidation

To rule out the possibility of a phase transition from semiconducting 2H to metallic 1T´, temperature-dependent Raman measurements are performed on as-exfoliated multilayer 2H-$MoTe_2$ flakes on a SiO_2/Si substrate. Raman spectra are recorded at various temperatures ranging from 303 K to 663 K with an interval of 20 K, as shown in the Figure 6.2a. Typically, a multilayer 2H-$MoTe_2$ flake exhibits prominent A_{1g} and E_{2g} peaks at 173 cm^{-1} and 233 cm^{-1} at room temperature, respectively. However, the Raman modes experience a redshift with increasing temperature, with the A_{1g} and E_{2g} modes' peak positions shifting by - 4 cm^{-1} and - 8 cm^{-1} at 663 K, respectively. This shift is attributed to the high-temperature-induced thermal expansion of the lattice and anharmonic phonon coupling in $MoTe_2$. Crucially, the Raman signals from the samples at elevated temperatures do not exhibit any trace of the 1T´ phase of $MoTe_2$, which typically has characteristic Raman modes at 125 cm^{-1} and 140 cm^{-1}[164], [165]. Therefore, these results suggest that a $MoTe_2$ phase transition does not occur within this temperature range and provide more insight into the unusual transfer characteristics observed in $MoTe_2$ at high temperatures.

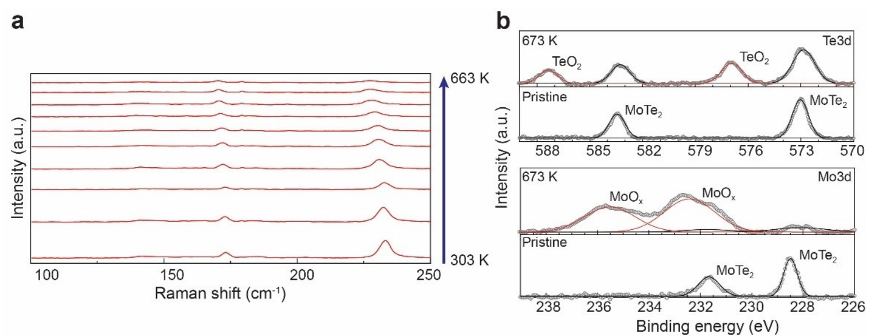

Figure 6.2. Physical properties of $MoTe_2$ at high temperatures. (a) Temperature-dependent Raman spectra of the $MoTe_2$ sample with a temperature range from 303 K to 663 K. (b) XPS core level spectra for Mo3*d* and Te3*d* from pristine and $MoTe_2$ flakes thermally treated at 673 K. Adapted from **Publication III.**

In these experiments, $MoTe_2$ devices exhibit an extremely low μ of ~ 1 $cm^2V^{-1}s^{-1}$, which is significantly below the theoretically predicted phonon-

limited μ of ~ 200 $cm^2V^{-1}s^{-1}$[166]. This substantial difference suggests the presence of numerous defects in the channel, including thermally induced Te vacancies in $MoTe_2$[44], [45]. If the device is operated in the ambient conditions, there is a high possibility that oxygen will form Mo-O and Te-O bonds at elevated temperatures, initiating surface passivation through oxidation. These defects can introduce acceptor-type trap states near the valence band edge, which could explain the hole-dominated transport in $MoTe_2$ devices. To gain a comprehensive understanding of the defect formation process, XPS analysis is performed to investigate the surface chemical composition of $MoTe_2$ before and after thermal treatments. Figure 6.2b presents the core-level XPS spectra of Mo-3*d* and Te-3*d* collected from pristine and $MoTe_2$ flakes thermally treated at 673 K. In the lower panel, pristine $MoTe_2$ displays a Mo-3*d* doublet at 231.6 eV (Mo-3$d_{3/2}$) and 228.4 eV (Mo-3$d_{5/2}$), representing characteristic of $MoTe_2$. However, after annealing at 673 K, two new peaks appear at 235.5 eV and 232.3 eV, corresponding to Mo-3$d_{3/2}$ and Mo-3$d_{5/2}$ modes of MoO_3, respectively. In the upper panel, Te-3*d* doublet peaks for pristine $MoTe_2$ are found at 583.3 eV (Te-3$d_{3/2}$) and 573 eV (Te-3$d_{5/2}$). Following the 673 K annealing, a new doublet appears at 587 eV and 576.7 eV, consistent with TeO_2. These new peaks, along with the weaker $MoTe_2$ peaks, indicate a substantial conversion of the top surface of $MoTe_2$ to MoO_x and TeO_2 at elevated temperatures.

6.1.3 Hopping transport in $MoTe_2$ devices

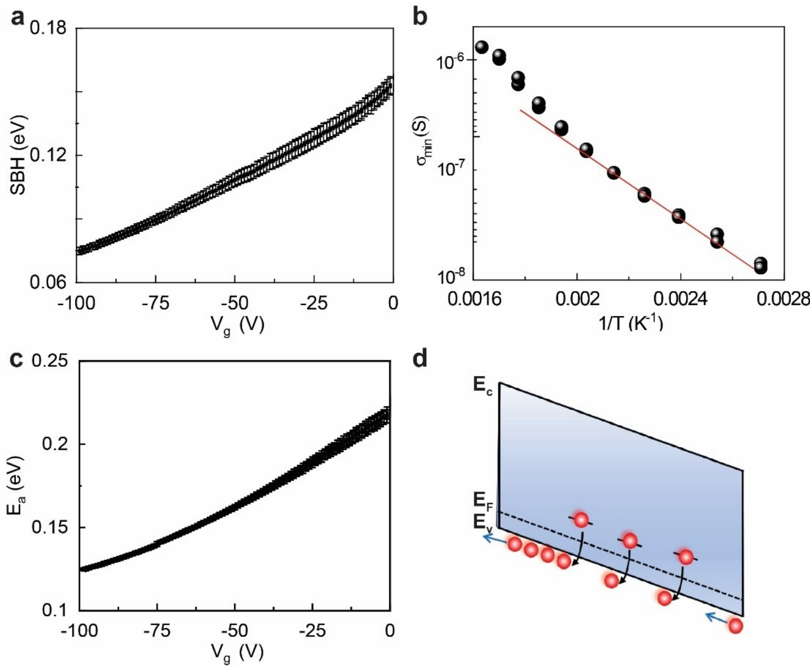

Figure 6.3. Carrier transport mechanism in the defective $MoTe_2$ channel. **(a)** Variation of the SBH in $MoTe_2$ devices with Ni contacts as a function of V_g. **(b)** Inverse-temperature dependent channel conductance at V_g = 100 V with the red line representing thermally activated NNH transport. **(c)** Change in activation energy in the device at different V_g

values. **(d)** Hopping transport mechanism in $MoTe_2$ FET at high temperatures. Adapted from **Publication III.**

In defective 2D devices with channel-dominated transport, charge carriers localize around defect sites and they transport through a hopping mechanism. To confirm channel-dominant transport in our $MoTe_2$ devices, the SBH is measured at the metal/$MoTe_2$ interface using the thermionic emission model, as shown in Figure 6.3a. The effective SBH values are decreased from 0.15 eV at V_g = 0 to 0.075 eV at V_g = -100 V. This result confirms the p-type nature of $MoTe_2$ device and the presence of channel-dominant transport due to small values of SBH. Hopping transport is further confirmed by extracting the conductance using $\sigma \propto \exp[-(T_0/T)^{\gamma}]$, where T is variable temperature, T_0 is the ambient temperature, and γ is a constant and it varies within the range from 0.25 to 1 depending on the system dimensionality[167]. Figure 6.3b shows σ as a function of temperature ranging from 373 to 625 K at V_g = 100 V. At elevated temperatures, σ changes with a γ value of 1, indicating the disordered $MoTe_2$ channel and thermally activated near neighbor hopping transport. Additionally, the activation energy (E_a) is calculated using $\sigma \propto \exp[-(E_a/k_B T)^{\gamma}]$, where k_B represents the Boltzmann constant, and plotted against V_g in Figure 6.3c[167]–[169]. The extracted E_a values varied from 0.22 to 0.12 eV, suggesting the depth of charge traps near the valence band maxima. These traps are likely associated with oxide defects rather than Te vacancies[170], as $MoTe_2$ devices exhibit more p-type behavior at high temperatures. The temperature increase allows trapped charge carriers to gain sufficient energy to hop over the energy barrier, contributing to conduction, as illustrated with a schematic in Figure 6.3d. Therefore, high-temperature measurements demonstrate increased current density, conductivity, and carrier mobility.

6.2 Effect of strain and doping

6.2.1 Carrier mobility enhancement

In this study, the impact of local strain on $MoTe_2$ is investigated by creating a hole array pattern on a SiO_2/Si substrate and taking advantage of ALD-grown metal-oxide layers on the material. The hole-array pattern simplifies the device fabrication process, making it easier to utilize the benefits of metal oxide and conveniently apply strain to the material. Firstly, hole arrays having various hole diameters are fabricated on a SiO_2/Si substrate. Subsequently, a 5 nm thick Al_2O_3 layer is grown onto the substrate which covers the whole substrate including the holes. Following this, $MoTe_2$ flakes are transferred onto the hole-array substrate using the hot pick-up technique[105]. The uniformity and high quality of the Al_2O_3 layer produced by layer-by-layer deposition process in the ALD reactor contribute to the good adhesion of $MoTe_2$ with the substrate. $MoTe_2$ FETs with Au/Ti contacts are created on this substrate, and an additional 50 nm Al_2O_3 layer is deposited onto the devices using a seeding layer afterward. The seed layer ensures good coverage of Al_2O_3 on the $MoTe_2$ because 2D materials have no dangling bonds on the surface. Figure 6.4a provides a schematic representation of the device structure, with the holes on the substrate measuring 200 nm in diameter and around 50 nm in depth after the deposition of the 5 nm

Al_2O_3 layer. AFM depth profiles with the corresponding AFM images and optical image of a sample are presented in Figure 6.4b for a better understanding of the morphology of the devices.

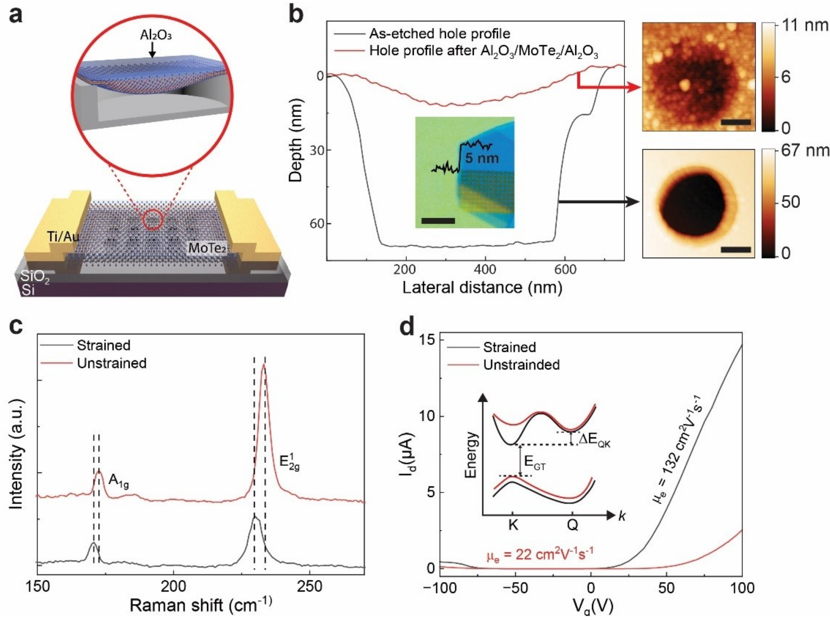

Figure 6.4. Fabrication and performance analysis of $MoTe_2$ FET. **(a)** Schematic of a FET showing strain in $MoTe_2$ by hole array in the SiO_2 and passivation of Al_2O_3. **(b)** Depth profiles of before and after the transfer of $MoTe_2$ transfer and 50 nm Al_2O_3 passivation. Corresponding depth AFM images are shown with black and red arrows with a scale bar of 100 nm for both images. The inset shows the optical image and thickness profile of the MoT_2 flake. Scale bar: 5 µm. **(c)** Raman peak position shift comparison between strained and unstrained samples. **(d)** Transfer curves and corresponding μ_e values of strained and unstrained $MoTe_2$ devices. A simplified $MoTe_2$ band diagram schematic before and after the application of strain is presented in the inset. E_{GT} and ΔE_{QK} represent the band gap and conduction band energy difference between K point and Q point in unstrained (red lines) and strained (black lines) $MoTe_2$, respectively. Adapted from **Publication IV.**

A 532 nm laser is used for Raman measurements to investigate strain in $MoTe_2$ samples. The objective is to characterize the nature and magnitude of strain in both strained and unstrained $MoTe_2$ samples. The presence of distinct Raman peaks of $MoTe_2$ (E_{2g}^1 and A_{1g}) in both samples confirms the high quality of the $MoTe_2$ flakes. It is observed that the Raman modes in the strained $MoTe_2$ samples exhibited redshifts of approximately 2.98 cm^{-1} and 2.22 cm^{-1} for the E_{2g}^1 and A_{1g} modes, respectively, and lower intensities in comparison to the unstrained regions of the flakes, as depicted in Figure 6.4c. These findings are consistent with previous reports[140], [141], [171]. Notably, these studies had reported nearly negligible shifts in the A_{1g} mode under tensile strain. The observed A_{1g} mode shift in strained $MoTe_2$ in this case, can be attributed to the use of few-layer and unsupported $MoTe_2$ or the effects of altered dielectric environments[139] in the hole-array regions of our samples. Another contributing factor to this larger shift could be the high level of doping induced in $MoTe_2$ by

Al_2O_3[140], [172], [173]. Additionally, the estimated magnitude of strain according to the shift in the E^1_{2g} mode is ~ 0.67 %[141].

The impact of the hole-array pattern and the top Al_2O_3 layer-induced strain in the performance of $MoTe_2$ FETs is analyzed afterward. The local tensile strain introduced by the structure significantly enhances the electron current and μ in $MoTe_2$ FETs by up to ~ 6 times compared to unstrained samples, as depicted in Figure 6.4d. The modification in the band structure of MoT_2 due to the strain results in reduced electron-phonon scattering, thereby enhancing the electrical response from the FETs. As illustrated in the inset of Figure 6.4d, the bandgap (E_{GT}) of $MoTe_2$ decreases and lowers the valley of the conduction band at the K point upon applying strain to the few-layer $MoTe_2$ flake. Consequently, the energy difference between the K point and the Q point (represented as ΔE_{QK}) increases, resulting in minimal electron intervalley scattering due to a reduction in the electron effective mass. This could be the key factor behind the elevated μ_e in $MoTe_2$ FETs. Moreover, the contact resistance decreases as the SBH decreases with strain in 2D materials and contributes further to the higher μ_e. The carrier lifetimes in $MoTe_2$ can be extended significantly by reducing charge carrier trapping through the application of strain, which can also be a contributing factor for high mobility in the devices.

Figure 6.5a presents the hole diameter-dependent mobility *EF* showing an increase in mobility of the devices with increasing hole diameters and the height *EF* is recorded with 300 nm diameter holes. A similar *EF* value is also observed at a 200 nm diameter. However, as the hole diameter expands to 400 nm, the *EF* starts to decrease which could be the reason for increasing flat regions at the center of the $MoTe_2$ flake, resulting in less overall strain on the sample. This mobility *EF* trend follows the hole diameter-dependent Raman peak shifts of E^1_{2g} and A_{1g} modes observed in Figure 6.5b. These findings indicate that the tensile strain induced by the hole-array pattern on the substrate coupled with the top Al_2O_3 layer remarkably enhances the performance of $MoTe_2$ devices.

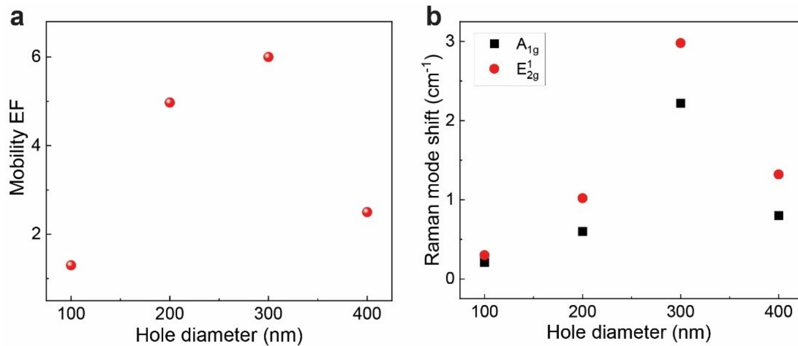

Figure 6.5. Effect of hole diameter on $MoTe_2$ electron mobility. **(a)** Hole diameter dependency of the enhancement factor *EF* in the devices. **(b)** Raman mode shifts as a function of hole diameters. Adapted from **Publication IV.**

6.2.2 Polarity of strained $MoTe_2$ devices

Typically, when Al_2O_3 is deposited through ALD, it induces n-doping in 2D materials. This is especially noticeable in the electrical behavior of 2D FETs when compared to bare 2D FETs on SiO_2/Si substrates. Al_2O_3 effectively dopes the material by injecting electrons into the channel, resulting in a modulation in carrier type. For example, Al_2O_3 can convert p-type material to p-dominant, n-dominant ambipolar, or even to n-type. This doping also increases in the current level and μ_e in the devices. Additionally, Al_2O_3 also provides a superior interface and protection from external absorbents from the top, which may also contribute to reduce the hysteresis and an enhancement in μ_h in the devices.

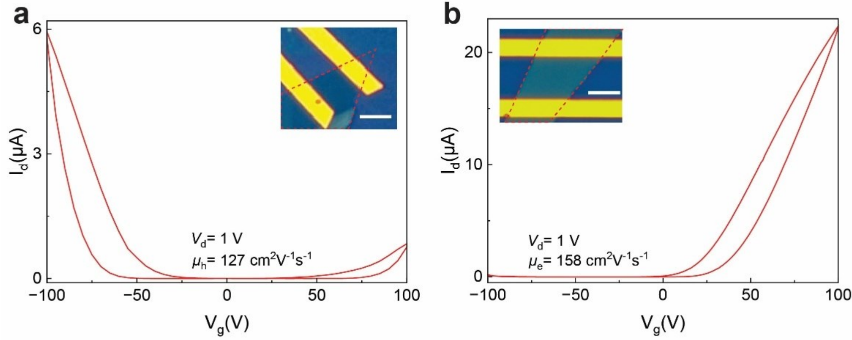

Figure 6.6. Electrical responses of strained $MoTe_2$ devices. Transfer characteristics of **(a)** a ~2.7 nm thick p-dominant ambipolar FET with μ_h, and **(b)** a ~ 5.8 nm thick n-type device with μ_e. $V_d = 1\ V$ is used for both measurements. The corresponding device images are shown as insets in each figure while both images contain 3 μm scale bars. Adapted from **Publication IV.**

In this study, it has been observed that thinner $MoTe_2$ flakes typically exhibit p-type behavior, while relatively thicker flakes display n-type characteristics. Figures 6.6a and b depict the transfer curves of ~ 2.7 nm and ~ 5.8 nm thick $MoTe_2$ flakes, respectively, which are transferred onto a hole array pattern and passivated with a 50 nm Al_2O_3 layer. The thinner flakes exhibit p-dominant ambipolar behavior, while the thicker flake displays n-type behavior, having μ_h of ~127 $cm^2V^{-1}s^{-1}$ and μ_e of ~158 $cm^2V^{-1}s^{-1}$, respectively. These mobility values are calculated using Equation 4.1 in which a 5 nm Al_2O_3 layer and 285 nm SiO_2 layer are used as dielectric materials. It is important to note that these mobility values are extracted from 2PP measurements, which typically underestimate mobility due to the influence of contact resistance. 4PP measurement is needed to have a more accurate assessment of carrier mobilities in these devices.

6.2.3 Metal-insulator transition

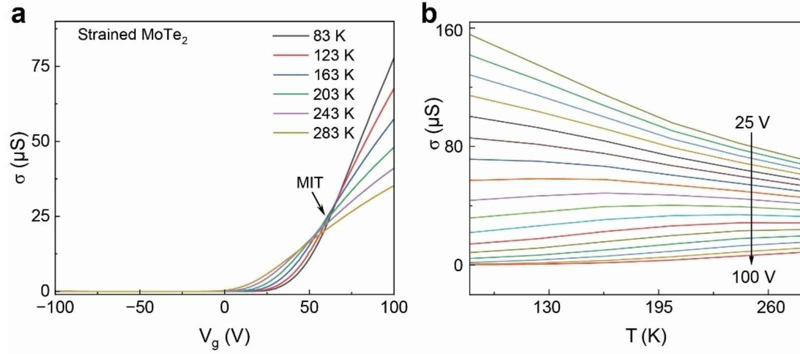

Figure 6.7. Temperature-dependent transport in strained $MoTe_2$ devices. **(a)** Conductance (σ) of the device for different V_g at various temperatures. The MIT point is shown with an arrow. **(b)** Temperature-dependent σ at different V_g values ranging from 25 V to 100 V. Adapted from **Publication IV.**

The transfer characteristics of n-type $MoTe_2$ transistors with Au/Ti contacts are examined at various temperatures. Remarkably, a distinct metal-insulator transition (MIT) phenomenon is observed in these $MoTe_2$ devices[174], [175]. The I_d-V_g curve shows a crossover occurring at a specific V_g, known as the MIT point (at V_g = 62 V), as shown in Figure 6.7a. Below this threshold point, the $MoTe_2$ device conductivity increases as the temperature rises, indicating insulating behavior. Conversely, conductivity decreases as the temperature rises above the MIT point, signifying metallic behavior. The estimated carrier density is $n_D \sim 3.74 \times 10^{-12}\ cm^{-2}$ at the MIT point. This is calculated using $n_D = \frac{C_{ox}(V_g - V_{th})}{q}$, where C_{ox} represents the total capacitance of the dielectrics, V_{th} and q stand for the threshold voltage and charge of an electron, respectively[176]. The temperature-dependent conductivity relationship is illustrated in Figure 6.7b. The MIT observed in $MoTe_2$ devices confirms their stability and high quality to ensure efficient modulation of electrical conductivity.

6.3 Phase modulation by optical writing

6.3.1 Influence on optical properties

$MoTe_2$ is a unique TMDC that requires relatively low energy (< 50 meV) to transition from the semiconducting 2H phase to the metastable metallic 1T´phase due to the small electronegativity difference (~ 0.3) between Mo and Te atoms[165], [177]. This low-phase transition barrier and its suitability for optical modification make it a promising candidate for advanced optoelectronic and photonic devices. In this study, a lithography-free and highly selective optical writing technique is exploited to convert 2H-$MoTe_2$ into 1T´ using a continuous-wave visible laser. This approach also enables the creation of high-performance optoelectronic and photonic devices.

Laser-induced thermal energy can induce an irreversible phase transition from 2H to 1T′ in $MoTe_2$ by increasing the local temperature of the flake and

creating Te vacancies. Polymorphism in $MoTe_2$ is achieved by irradiating a continuous-wave 532 nm laser with a power of ~ 9 mW in atmospheric conditions. Figure 6.8a illustrates a schematic of an optical writing process using a laser on 2H $MoTe_2$, which is mounted onto a piezo-driven stage to convert a selective area resembling the Aalto University logo (A!) into the 1T´ phase. The piezo-stage of the optical setup ensures feature selectivity with a resolution of approximately 0.7 µm (1.2 λ/N.A., where λ = 532 nm and N.A. = 0.9). The bright and dark-field optical images after laser exposure are presented in Figures 6.8b and c, respectively. The characteristic Raman spectra are recorded from the sample's 2H and phase-converted 1T´ regions and shown in Figure 6.8d. A_{1g} and E_{2g} peaks of 2H-$MoTe_2$ are observed at 171 and 235 cm^{-1} while the vibrational modes (A_g) of 1T´phase are appeared at 121 and 140 cm^{-1} from laser irradiated area[164]. A Raman map centering at 121 cm^{-1} is presented in the inset of Figure 6.8c. Micro-reflection analysis is another effective technique for determining the phase transition in 2D materials. Figure 6.8e shows the measurement results in the near-infrared region taken from both the 2H and 1T´ areas of a $MoTe_2$ flake. The optical image of the multi-layered flake is shown in the inset of figure. The reflectance spectrum of 2H-$MoTe_2$ exhibits an excitonic transition at ~1300 nm (~1 eV). In contrast, this excitonic transition dip is absent in 1T´-$MoTe_2$, and the reflectance is also lower than that of 2H-$MoTe_2$. These results further confirm the phase transition in $MoTe_2$.

Additionally, the phase changed 1T´-$MoTe_2$ exhibits an unprecedented nonlinear optical response. The THG response measured from 1T´-$MoTe_2$ shows ~ 7 times stronger signal compared to 2H-$MoTe_2$. Moreover, the measured THG conversion efficiency for 1T′-$MoTe_2$ is ~ 1.7×10^{-7}, whereas it is ~ 1.7×10^{-8} in 2H-$MoTe_2$. In addition, the calculated effective third-order susceptibilities are 1.1×10^{-19} $m^2 V^{-2}$ for 1T′-phase and 0.3×10^{-19} $m^2 V^{-2}$ for 2H-phase. The enhanced THG in 1T′-$MoTe_2$ can be attributed to its higher absorption at the pump wavelength of 1500 nm, as shown in Figure 6.8e. The generation of tellurium vacancies induced by the laser may also have contributed to the increased THG intensity in 1T′-$MoTe_2$. These results open up new application possibilities for $MoTe_2$ in ultrafast lasers, saturable absorbers, and broadband light conversion.

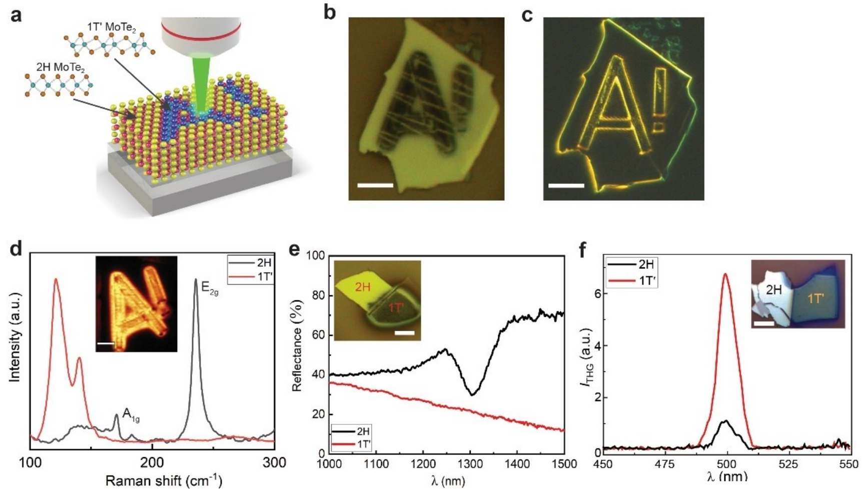

Figure 6.8. Modulation of polymorphs in $MoTe_2$. **(a)** Schematic representation of optical writing for converting 2H-$MoTe_2$ to 1T´. The crystal structures of both phases are indicated by arrows pointing toward the corresponding areas on the $MoTe_2$ flake. **(b)** Bright-field and **(c)** Dark field image of the laser-irradiated multilayer $MoTe_2$ flake. The scale bar for both images is 5 μm. **(d)** Raman spectra of 2H and 1T´ from the sample. The inset shows Raman intensity maps of the 1T´ mode of $MoTe_2$ after phase conversion using a 532 nm laser. Scale bar: 5 μm. **(e)** Reflectance spectra from 2H and 1T´ regions of the $MoTe_2$ flake. The corresponding flake is presented in the inset, where the greenish area represents the 2H-$MoTe_2$ part, and the black region of the flake is the converted 1T´ region. **(f)** Comparison of the THG signals from 2H and 1T´ $MoTe_2$. The optical image of the partially converted flake is shown in the inset. Scale bar: 10 μm. Adapted from **Publication V.**

6.3.2 Enhancement of optoelectronic properties

Unlike conventional p-n junction diodes, metal-semiconductor diodes offer doping-free fabrication, low power consumption, and low dark current in optoelectronic devices. Leveraging the polymorphic characteristics of $MoTe_2$, Schottky diodes can be realized by introducing metallic and semiconducting $MoTe_2$ into the same channel through optical writing to create a metal-semiconductor junction, as shown in Figure 6.9a. A shift in I_{Ph} minima towards positive V_d, along with an increase in zero bias current, is observed in the I_{Ph} vs. laser (532 nm) power plot in Figure 6.9b. These responses suggest that the Schottky diode acts as a photovoltaic cell with a good open-circuit voltage and short-circuit current under specific light conditions. The obtained R and D^* values are presented in Figure 6.9c. Remarkably, the device demonstrates R of 90 AW^{-1} and D^* of 10^9 Jones at 0.1 W cm^2 power density. These values decrease with higher illumination power because photoexcited charge carrier generation saturates at higher power levels. Notably, these values surpass reported values for $MoTe_2$-based photodetectors.

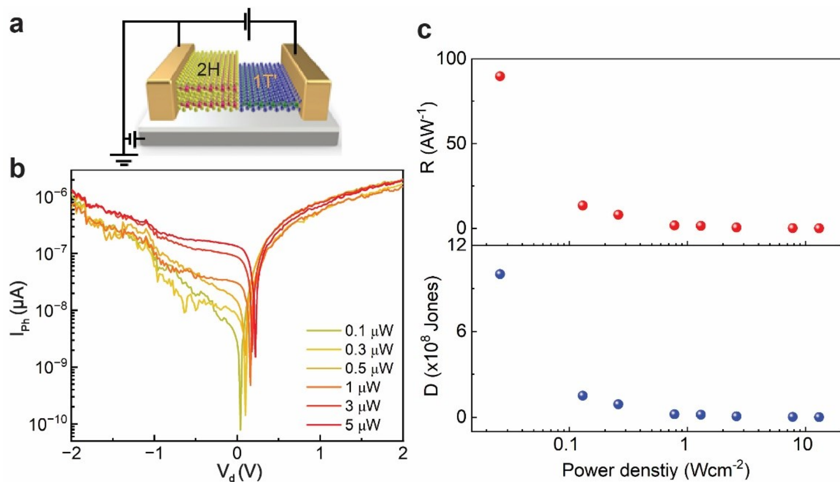

Figure 6.9. Optoelectronic properties of the 2H-1T' junction in $MoTe_2$. **(a)** Schematic of the device. **(b)** I_{Ph} at various 532 nm laser powers. **(c)** *R* and *D** of the device concerning laser power density. Adapted from **Publication V.**

7. Conclusion

Over the last decade, 2D layered TMDCs have emerged as promising candidates for both replacing and complementing silicon technology in the fields of photonics and electronics. This is primarily attributed to their remarkable ability to exhibit tunable electronic and optical properties. Despite significant efforts to functionalize TMDCs for practical device applications in recent years, there are substantial opportunities for enhancing their fundamental properties due to inherent limitations in their behaviors. With this motivation, this thesis explores fundamental characteristics of TMDCs and aims to enhance their properties through mixed-dimensional heterostructures, strain engineering, doping, and phase modulation techniques.

Mixed-dimensional heterostructures can improve light-matter interactions, leading to the development of high-performance photonic and optoelectronic devices. This thesis investigates two types of mixed-dimensional heterostructures. Firstly, a mixed-dimensional heterostructure is created by transferring monolayer MoS_2 onto NW_{AlGaAs} for utilizing the nanowires' EM field confinement property to enhance optical responses from MoS_2. Raman and PL from MoS_2/NW_{AlGaAs} are enhanced by ~ 3 and ~ 9 times, respectively, compared to bare MoS_2. The heterostructure also exhibits ~ 60 % optical anisotropy due to the C_3 rotational symmetry breaking in MoS_2 caused by the nanowires. Additionally, the fabricated phototransistor using the heterostructure shows improved performance with polarization sensitivity. Secondly, another mixed-dimensional heterostructure is formed by epitaxially growing NW_{InP} directly on MoS_2 to harness the strong nonlinear properties of both materials. High-density vertical growth of nanowires on MoS_2 is achieved while ensuring the chemical and thermal stability of MoS_2. These heterostructures exhibit strong SHG and THG signals, along with remarkable 5th and 7th HHG signals. The nonlinearity in the NW_{InP}/MoS_2 heterostructure has the potential to create opportunities for numerous applications, such as lasers, electro-optic modulators, and frequency converters.

In the following part of the thesis, electronic properties of TMDCs are tuned for fabricating high-performance electronic and optoelectronic devices. $MoTe_2$, a TMDC with significant potential in electronic applications, is extensively studied due to its limitations such as high sensitivity to environmental factors, low carrier mobilities, and relatively weak optoelectronic responses. To start with, the effect of high temperature on multilayer-$MoTe_2$ devices is systematically examined by designing two sets of experiments: one examining device responses

after annealing at various temperatures and another assessing device performance at high temperatures. From the multistep annealing process, the optimum annealing temperature is determined (~ 500 K) for $MoTe_2$ FETs. On the other hand, the high-temperature measurements demonstrate the effect of thermally induced defects due to surface oxidation of $MoTe_2$ and the hopping transport mechanism in the defective channel of the devices. These findings shed light on the development of practical 2D TMDC-based devices for practical electronic applications.

Subsequently, a facile technique for enhancing the performance of a few-layer $MoTe_2$ devices is demonstrated. The technique involves creating hole arrays on the substrate and employing ALD-grown Al_2O_3 as additional dielectric and passivation layers for the $MoTe_2$ channel. This structure introduces local tensile strain on $MoTe_2$, which modifies the band structure of the material and reduces the electron-phonon scattering in the sample. Consequently, the hole and electron mobilities in the devices increased up to ~ 130 and 160 $cm^2V^{-1}s^{-1}$, respectively. Notably, the electron mobility is enhanced by ~ 6 times compared to the unstrained device. Furthermore, a well-defined MIT is observed in the strained devices that ensures the high quality of the strained $MoTe_2$ FETs. The proposed structure shows great potential to address the low-performance limitations in TMDC-based electronic devices.

Finally, polymorphic characteristics of $MoTe_2$ are modulated using a simple optical writing technique to tune the photonic and optoelectronic properties of $MoTe_2$. The semiconducting 2H phase of $MoTe_2$ is transformed into the metallic 1T´ phase by irradiating the samples with a visible-range laser. As a result of this phase transition, 1T´-$MoTe_2$ exhibits approximately sevenfold improvement in THG nonlinear optical signals compared to 2H-$MoTe_2$. Additionally, a Schottky diode fabricated with 2H-$MoTe_2$ and converted 1T´-$MoTe_2$ in the same flake demonstrates excellent responsivity and detectivity. Polymorphism engineering using this proposed technique holds great promise for advancing integrated photonic and optoelectronic circuits based on 2D-TMDCs.

References

[1] K. S. Novoselov *et al.*, “Electric Field Effect in Atomically Thin Carbon Films,” *Science (80-.).*, vol. 306, no. 5696, pp. 666–669, Oct. 2004.

[2] A. J. Mannix, B. Kiraly, M. C. Hersam, and N. P. Guisinger, “Synthesis and chemistry of elemental 2D materials,” *Nat. Rev. Chem.*, vol. 1, pp. 1–15, 2017.

[3] A. K. Geim and K. S. Novoselov, “The rise of graphene,” *Nat. Mater.*, vol. 6, no. 3, pp. 183–191, Mar. 2007.

[4] F. Bonaccorso, Z. Sun, T. Hasan, and A. C. Ferrari, “Graphene photonics and optoelectronics,” *Nat. Photonics*, vol. 4, no. 9, pp. 611–622, 2010.

[5] S. Manzeli, D. Ovchinnikov, D. Pasquier, O. V. Yazyev, and A. Kis, “2D transition metal dichalcogenides,” *Nat. Rev. Mater.*, vol. 2, 2017.

[6] B. Radisavljevic, A. Radenovic, J. Brivio, V. Giacometti, and A. Kis, “Single-layer MoS_2 transistors,” *Nat. Nanotechnol.*, vol. 6, no. 3, pp. 147–150, 2011.

[7] K. F. Mak, C. Lee, J. Hone, J. Shan, and T. F. Heinz, “Atomically thin MoS_2: A new direct-gap semiconductor,” *Phys. Rev. Lett.*, vol. 105, no. 13, p. 136805, Apr. 2010.

[8] A. Splendiani *et al.*, “Emerging photoluminescence in monolayer MoS_2,” *Nano Lett.*, vol. 10, no. 4, pp. 1271–1275, 2010.

[9] L. Tao, Z. Chen, Z. Li, J. Wang, X. Xu, and J. Xu, “ Enhancing light-matter interaction in 2D materials by optical micro/nano architectures for high-performance optoelectronic devices ,” *InfoMat*, vol. 3, no. 1, pp. 36–60, 2021.

[10] M. Amani *et al.*, “Near-unity photoluminescence quantum yield in MoS_2,” *Science (80-.).*, vol. 350, no. 6264, pp. 1065–1068, 2015.

[11] L. Zhao, Q. Shang, M. Li, Y. Liang, C. Li, and Q. Zhang, “Strong exciton-photon interaction and lasing of two-dimensional transition metal dichalcogenide semiconductors,” *Nano Res.*, vol. 14, no. 6, pp. 1937–1954, 2021.

[12] L. Huang, A. Krasnok, A. Alú, Y. Yu, D. Neshev, and A. E. Miroshnichenko, “Enhanced light-matter interaction in two-dimensional transition metal dichalcogenides,” *Reports on Progress in Physics*, vol. 85, no. 4. p. 046401, Apr. 01, 2022.

[13] X. Huang *et al.*, “Fabry-Perot cavity enhanced light-matter interactions in two-dimensional van der Waals heterostructure,” *Nano Energy*, vol. 62, no. June, pp. 667–673, Aug. 2019.

[14] J. F. Gonzalez Marin, D. Unuchek, K. Watanabe, T. Taniguchi, and A. Kis, “MoS_2 photodetectors integrated with photonic circuits,” *npj 2D Mater. Appl.*, vol. 3, no. 1, 2019.

[15] Y. Dai *et al.*, “Broadband Plasmon-Enhanced Four-Wave Mixing in Monolayer MoS_2,” *Nano Lett.*, vol. 21, no. 14, pp. 6321–6327, Jul. 2021.

[16] Q. Ren *et al.*, “Multiplexing-oriented plasmon-MoS_2 hybrid metasurfaces driven by nonlinear quasi bound states in the continuum,” *Opt. Express*,

vol. 29, no. 4, p. 5384, Feb. 2021.

[17] A. I. Kuznetsov, A. E. Miroshnichenko, M. L. Brongersma, Y. S. Kivshar, and B. Luk'yanchuk, "Optically resonant dielectric nanostructures," *Science (80-.).*, vol. 354, no. 6314, 2016.

[18] A. F. Cihan, A. G. Curto, S. Raza, P. G. Kik, and M. L. Brongersma, "Silicon Mie resonators for highly directional light emission from monolayer MoS2," *Nat. Photonics*, vol. 12, no. 5, pp. 284–290, 2018.

[19] A. M. Shafi *et al.*, "Inducing Strong Light-Matter Coupling and Optical Anisotropy in Monolayer MoS2with High Refractive Index Nanowire," *ACS Appl. Mater. Interfaces*, vol. 14, no. 27, pp. 31140–31147, 2022.

[20] J. Johansson *et al.*, "Structural properties of 〈111〉 B -oriented III-V nanowires," *Nat. Mater.*, vol. 5, no. 7, pp. 574–580, 2006.

[21] S. K. Lim, M. Brewster, F. Qian, Y. Li, C. M. Lieber, and S. Gradečak, "Direct correlation between structural and optical properties of III - V nitride nanowire heterostructures with nanoscale resolution," *Nano Lett.*, vol. 9, no. 11, pp. 3940–3944, 2009.

[22] L. Hrachowina, N. Anttu, and M. T. Borgström, "Wafer-Scale Synthesis and Optical Characterization of InP Nanowire Arrays for Solar Cells," *Nano Lett.*, vol. 21, no. 17, pp. 7347–7353, 2021.

[23] N. Anttu, H. Mäntynen, T. Sadi, A. Matikainen, J. Turunen, and H. Lipsanen, "Comparison of absorption simulation in semiconductor nanowire and nanocone arrays with the Fourier modal method, the finite element method, and the finite-difference time-domain method," *Nano Express*, vol. 1, no. 3, p. 030034, 2020.

[24] J. C. Shin *et al.*, "Heterogeneous integration of InGaAs nanowires on the rear surface of Si solar cells for efficiency enhancement," *ACS Nano*, vol. 6, no. 12, pp. 11074–11079, 2012.

[25] V. Dhaka *et al.*, "High quality GaAs nanowires grown on glass substrates," *Nano Lett.*, vol. 12, no. 4, pp. 1912–1918, 2012.

[26] V. Khayrudinov *et al.*, "Direct Growth of Light-Emitting III-V Nanowires on Flexible Plastic Substrates," *ACS Nano*, vol. 14, no. 6, pp. 7484–7491, Jun. 2020.

[27] P. K. Mohseni *et al.*, "InxGa1-xas nanowire growth on graphene: Van der waals epitaxy induced phase segregation," *Nano Lett.*, vol. 13, no. 3, pp. 1153–1161, Mar. 2013.

[28] Y. Berdnikov *et al.*, "Growth of GaAs nanowire-graphite nanoplatelet hybrid structures," *CrystEngComm*, vol. 21, no. 41, pp. 6165–6172, 2019.

[29] Y. J. Hong, W. H. Lee, Y. Wu, R. S. Ruoff, and T. Fukui, "Van der Waals epitaxy of InAs nanowires vertically aligned on single-layer graphene," *Nano Lett.*, vol. 12, no. 3, pp. 1431–1436, 2012.

[30] M. A. Baboli *et al.*, "Mixed-dimensional InAs nanowire on layered molybdenum disulfide heterostructures: Via selective-area van der Waals epitaxy," *Nanoscale Adv.*, vol. 3, no. 10, pp. 2802–2811, 2021.

[31] A. M. Shafi *et al.*, "Direct Epitaxial Growth of InP Nanowires on MoS_2 with Strong Nonlinear Optical Response," *Chem. Mater.*, vol. 34, no. 20, pp. 9055–9061, 2022.

[32] Y.-F. Lin *et al.*, "Ambipolar MoTe 2 Transistors and Their Applications in Logic Circuits," *Adv. Mater.*, vol. 26, no. 20, pp. 3263–3269, May 2014.

[33] S. Ahmed and J. Yi, "Two-Dimensional Transition Metal Dichalcogenides and Their Charge Carrier Mobilities in Field-Effect Transistors," *Nano-*

Micro Lett., vol. 9, no. 4, p. 50, Oct. 2017.

[34] S. Nakaharai, M. Yamamoto, K. Ueno, Y.-F. Lin, S.-L. Li, and K. Tsukagoshi, "Electrostatically Reversible Polarity of Ambipolar α-$MoTe_2$ Transistors," *ACS Nano*, vol. 9, no. 6, pp. 5976–5983, Jun. 2015.

[35] N. R. Pradhan *et al.*, "Field-Effect Transistors Based on Few-Layered α-$MoTe_2$," *ACS Nano*, vol. 8, no. 6, pp. 5911–5920, Jun. 2014.

[36] M. W. Iqbal *et al.*, "Tailoring the electrical properties of $MoTe_2$ field effect transistor via chemical doping," *Superlattices Microstruct.*, vol. 135, no. September, p. 106247, 2019.

[37] T. Liu *et al.*, "Crested two-dimensional transistors," *Nat. Nanotechnol.*, vol. 14, no. 3, pp. 223–226, 2019.

[38] I. M. Datye, A. Daus, R. W. Grady, K. Brenner, S. Vaziri, and E. Pop, "Strain-Enhanced Mobility of Monolayer MoS_2," *Nano Lett.*, vol. 22, no. 20, pp. 8052–8059, Oct. 2022.

[39] L. Liao, J. Bai, Y. Qu, Y. Huang, and X. Duan, "Single-layer graphene on Al_2O_3 /Si substrate: better contrast and higher performance of graphene transistors," *Nanotechnology*, vol. 21, no. 1, p. 015705, Jan. 2010.

[40] S. Kim *et al.*, "High-mobility and low-power thin-film transistors based on multilayer MoS_2 crystals," *Nat. Commun.*, vol. 3, no. 1, p. 1011, Aug. 2012.

[41] W. Chen, R. Liang, J. Wang, S. Zhang, and J. Xu, "Enhanced photoresponsivity and hole mobility of $MoTe_2$ phototransistors by using an Al_2O_3 high-κ gate dielectric," *Sci. Bull.*, vol. 63, no. 15, pp. 997–1005, 2018.

[42] A. M. Shafi, G. Uddin, X. Cui, F. Ali, and F. Ahmed, "Strain Engineering for Enhancing Carrier Mobility in $MoTe_2$ Field-Effect Transistors," vol. 2303437, pp. 1–7, 2023.

[43] E. Pop, "Energy dissipation and transport in nanoscale devices," *Nano Res.*, vol. 3, no. 3, pp. 147–169, Mar. 2010.

[44] H. Zhu *et al.*, "Defects and Surface Structural Stability of $MoTe_2$ under Vacuum Annealing," *ACS Nano*, vol. 11, no. 11, pp. 11005–11014, 2017.

[45] D. Rhodes, S. H. Chae, R. Ribeiro-Palau, and J. Hone, "Disorder in van der Waals heterostructures of 2D materials," *Nat. Mater.*, vol. 18, no. 6, pp. 541–549, 2019.

[46] D. Qu *et al.*, "Carrier-Type Modulation and Mobility Improvement of Thin $MoTe_2$," *Adv. Mater.*, vol. 29, no. 39, p. 1606433, Oct. 2017.

[47] F. Ahmed *et al.*, "Multilayer MoTe2 Field-Effect Transistor at High Temperatures," *Adv. Mater. Interfaces*, vol. 8, no. 22, p. 2100950, Nov. 2021.

[48] H. Bergeron, D. Lebedev, and M. C. Hersam, "Polymorphism in post-dichalcogenide two-dimensional materials," *Chem. Rev.*, vol. 121, no. 4, pp. 2713–2775, 2021.

[49] W. Li, X. Qian, and J. Li, "Phase transitions in 2D materials," *Nat. Rev. Mater.*, vol. 6, no. 9, pp. 829–846, 2021.

[50] D. Voiry, A. Mohite, and M. Chhowalla, "Phase engineering of transition metal dichalcogenides," *Chem. Soc. Rev.*, vol. 44, no. 9, pp. 2702–2712, 2015.

[51] J. H. Sung *et al.*, "Coplanar semiconductor-metal circuitry defined on few-layer $MoTe_2$ via polymorphic heteroepitaxy," *Nat. Nanotechnol.*, vol. 12, no. 11, pp. 1064–1070, 2017.

[52] Q. Wang *et al.*, "Optically reconfigurable metasurfaces and photonic devices based on phase change materials," *Nat. Photonics*, vol. 10, no. 1, pp. 60–65, 2016.

[53] M. Wuttig, H. Bhaskaran, and T. Taubner, "Phase-change materials for non-volatile photonic applications," *Nat. Photonics*, vol. 11, no. 8, pp. 465–476, 2017.

[54] K. A. N. Duerloo, Y. Li, and E. J. Reed, "Structural phase transitions in two-dimensional Mo-and W-dichalcogenide monolayers," *Nat. Commun.*, vol. 5, no. May, 2014.

[55] Y. C. Lin, D. O. Dumcenco, Y. S. Huang, and K. Suenaga, "Atomic mechanism of the semiconducting-to-metallic phase transition in single-layered MoS_2," *Nat. Nanotechnol.*, vol. 9, no. 5, pp. 391–396, 2014.

[56] R. Kappera *et al.*, "Phase-engineered low-resistance contacts for ultrathin MoS_2 transistors," *Nat. Mater.*, vol. 13, no. 12, pp. 1128–1134, 2014.

[57] S. T. M. Akkanen, H. A. Fernandez, and Z. Sun, "Optical Modification of 2D Materials: Methods and Applications," *Adv. Mater.*, vol. 34, no. 19, 2022.

[58] M. Wang, D. Li, K. Liu, Q. Guo, S. Wang, and X. Li, "Nonlinear Optical Imaging, Precise Layer Thinning, and Phase Engineering in MoTe2with Femtosecond Laser," *ACS Nano*, vol. 14, no. 9, pp. 11169–11177, 2020.

[59] F. Ahmed *et al.*, "Deterministic Polymorphic Engineering of $MoTe_2$ for Photonic and Optoelectronic Applications," *Adv. Funct. Mater.*, Apr. 2023.

[60] Paras *et al.*, "A Review on Low-Dimensional Nanomaterials: Nanofabrication, Characterization and Applications," *Nanomaterials*, vol. 13, no. 1, pp. 1–44, 2023.

[61] M. Bacon, S. J. Bradley, and T. Nann, "Graphene quantum dots," *Part. Part. Syst. Charact.*, vol. 31, no. 4, pp. 415–428, 2014.

[62] H. Sun, L. Wu, W. Wei, and X. Qu, "Recent advances in graphene quantum dots for sensing," *Mater. Today*, vol. 16, no. 11, pp. 433–442, 2013.

[63] X. T. Zheng, A. Ananthanarayanan, K. Q. Luo, and P. Chen, "Glowing graphene quantum dots and carbon dots: Properties, syntheses, and biological applications," *Small*, vol. 11, no. 14, pp. 1620–1636, 2015.

[64] C. Biswas and Y. H. Lee, "Graphene versus carbon nanotubes in electronic devices," *Adv. Funct. Mater.*, vol. 21, no. 20, pp. 3806–3826, 2011.

[65] L. Qiu and F. Ding, "Understanding Single-Walled Carbon Nanotube Growth for Chirality Controllable Synthesis," *Accounts Mater. Res.*, vol. 2, no. 9, pp. 828–841, 2021.

[66] Y. Ando, X. Zhao, H. Shimoyama, G. Sakai, and K. Kaneto, "Physical properties of multiwalled carbon nanotubes," *Int. J. Inorg. Mater.*, vol. 1, no. 1, pp. 77–82, 1999.

[67] S. Rathinavel, K. Priyadharshini, and D. Panda, "A review on carbon nanotube: An overview of synthesis, properties, functionalization, characterization, and the application," *Mater. Sci. Eng. B Solid-State Mater. Adv. Technol.*, vol. 268, no. January 2020, p. 115095, 2021.

[68] H. Wang *et al.*, "Graphene nanoribbons for quantum electronics," *Nat. Rev. Phys.*, vol. 3, no. 12, pp. 791–802, 2021.

[69] P. V. Shinde, A. Tripathi, R. Thapa, and C. Sekhar Rout, "Nanoribbons of

2D materials: A review on emerging trends, recent developments and future perspectives," *Coord. Chem. Rev.*, vol. 453, p. 214335, 2022.

[70] C. Jia, Z. Lin, Y. Huang, and X. Duan, "Nanowire Electronics: From Nanoscale to Macroscale," *Chem. Rev.*, vol. 119, no. 15, pp. 9074–9135, 2019.

[71] M. H. Huang *et al.*, "Room-temperature ultraviolet nanowire nanolasers," *Science (80-.).*, vol. 292, no. 5523, pp. 1897–1899, 2001.

[72] A. B. Greytak, C. J. Barrelet, Y. Li, and C. M. Lieber, "Semiconductor nanowire laser and nanowire waveguide electro-optic modulators," *Appl. Phys. Lett.*, vol. 87, no. 15, pp. 1–3, 2005.

[73] J. Wallentin *et al.*, "InP nanowire array solar cells achieving 13.8% efficiency by exceeding the ray optics limit," *Science (80-.).*, vol. 339, no. 6123, pp. 1057–1060, 2013.

[74] E. Barrigón, M. Heurlin, Z. Bi, B. Monemar, and L. Samuelson, "Synthesis and Applications of III-V Nanowires," *Chemical Reviews*, vol. 119, no. 15. pp. 9170–9220, Aug. 14, 2019.

[75] A. Li, J. Zou, and X. Han, "Growth of III-V semiconductor nanowires and their heterostructures," *Sci. China Mater.*, vol. 59, no. 1, pp. 51–91, 2016.

[76] M. J. Allen, V. C. Tung, and R. B. Kaner, "Honeycomb carbon: A review of graphene," *Chem. Rev.*, vol. 110, no. 1, pp. 132–145, 2010.

[77] A. K. Geim, "Graphene: Status and prospects," *Science*, vol. 324, no. 5934. pp. 1530–1534, Jun. 19, 2009.

[78] A. H. Castro Neto, F. Guinea, N. M. R. Peres, K. S. Novoselov, and A. K. Geim, "The electronic properties of graphene," *Rev. Mod. Phys.*, vol. 81, no. 1, pp. 109–162, 2009.

[79] G. Cassabois, P. Valvin, and B. Gil, "Hexagonal boron nitride is an indirect bandgap semiconductor," *Nat. Photonics*, vol. 10, no. 4, pp. 262–266, 2016.

[80] H. Yang, X. Wang, and X. Z. Li, "Exciton-polariton properties of hexagonal BN-based microcavity and their potential applications in BEC and superconductivity," *Phys. Rev. B*, vol. 104, no. 20, pp. 1–11, 2021.

[81] F. Ahmed *et al.*, "Dielectric Dispersion and High Field Response of Multilayer Hexagonal Boron Nitride," *Adv. Funct. Mater.*, vol. 28, no. 40, 2018.

[82] K. Zhang, Y. Feng, F. Wang, Z. Yang, and J. Wang, "Two dimensional hexagonal boron nitride (2D-hBN): Synthesis, properties and applications," *J. Mater. Chem. C*, vol. 5, no. 46, pp. 11992–12022, 2017.

[83] C. R. Dean *et al.*, "Boron nitride substrates for high-quality graphene electronics," *Nat. Nanotechnol.*, vol. 5, no. 10, pp. 722–726, 2010.

[84] A. K. Geim and I. V. Grigorieva, "Van der Waals heterostructures," *Nature*, vol. 499, no. 7459, pp. 419–425, Jul. 2013.

[85] K. Kośmider and J. Fernández-Rossier, "Electronic properties of the MoS_2-WS_2 heterojunction," *Phys. Rev. B*, vol. 87, no. 7, p. 075451, Dec. 2012.

[86] G. Li *et al.*, "Observation of Van Hove singularities in twisted graphene layers," *Nat. Phys.*, vol. 6, no. 2, pp. 109–113, Feb. 2010.

[87] J. Kunstmann *et al.*, "Momentum-space indirect interlayer excitons in transition-metal dichalcogenide van der Waals heterostructures," *Nat. Phys.*, vol. 14, no. 8, pp. 801–805, Aug. 2018.

[88] K. S. Novoselov, A. Mishchenko, A. Carvalho, and A. H. Castro Neto, "2D

materials and van der Waals heterostructures," *Science (80-.).*, vol. 353, no. 6298, 2016.

[89] D. Jariwala, T. J. Marks, and M. C. Hersam, "Mixed-dimensional van der Waals heterostructures," *Nat. Mater.*, vol. 16, no. 2, pp. 170–181, 2017.

[90] G. Konstantatos *et al.*, "Hybrid grapheneĝquantum dot phototransistors with ultrahigh gain," *Nat. Nanotechnol.*, vol. 7, no. 6, pp. 363–368, 2012.

[91] Q. N. D. Lung *et al.*, "Graphene/III–V Quantum Dot Mixed-Dimensional Heterostructure for Enhanced Radiative Recombinations via Hole Carrier Transfer," *Nano Lett.*, vol. 23, no. 8, pp. 3344–3351, Apr. 2023.

[92] C. Li *et al.*, "Enhanced Photoluminescence of Monolayer $MoSe_2$ in a Double Resonant Plasmonic Nanocavity with Fano Resonance and Mode Matching," *Laser Photonics Rev.*, vol. 16, no. 2, pp. 1–7, 2022.

[93] M. G. Uddin *et al.*, "Engineering the Dipole Orientation and Symmetry Breaking with Mixed-Dimensional Heterostructures," *Adv. Sci.*, vol. 9, no. 20, pp. 1–6, 2022.

[94] D. Li *et al.*, "Anisotropic Enhancement of Second-Harmonic Generation in Monolayer and Bilayer MoS_2 by Integrating with TiO2 Nanowires," *Nano Lett.*, vol. 19, no. 6, pp. 4195–4204, 2019.

[95] L. Tao, Z. Chen, Z. Li, and J. Wang, "Enhancing light-matter interaction in 2D materials by optical micro / nano architectures for high-performance optoelectronic devices," no. March 2020, pp. 36–60, 2021.

[96] W. Li and J. Li, "Ferroelasticity and domain physics in two-dimensional transition metal dichalcogenide monolayers," *Nat. Commun.*, vol. 7, 2016.

[97] D. H. Keum *et al.*, "Bandgap opening in few-layered monoclinic $MoTe_2$," *Nat. Phys.*, vol. 11, no. 6, pp. 482–486, 2015.

[98] O. V. Yazyev and A. Kis, "MoS_2 and semiconductors in the flatland," *Mater. Today*, vol. 18, no. 1, pp. 20–30, Jan. 2015.

[99] F. Ahmed *et al.*, "Multilayer $MoTe_2$ Field-Effect Transistor at High Temperatures," *Adv. Mater. Interfaces*, vol. 8, no. 22, 2021.

[100] P. Johari and V. B. Shenoy, "Tuning the electronic properties of semiconducting transition metal dichalcogenides by applying mechanical strains," *ACS Nano*, vol. 6, no. 6, pp. 5449–5456, 2012.

[101] Z. He and W. Que, "Molybdenum disulfide nanomaterials: Structures, properties, synthesis and recent progress on hydrogen evolution reaction," *Appl. Mater. Today*, vol. 3, pp. 23–56, 2016.

[102] A. Taffelli, S. Dirè, A. Quaranta, and L. Pancheri, "MoS_2 based photodetectors: A review," *Sensors*, vol. 21, no. 8, 2021.

[103] P. Budania *et al.*, "Comparison between Scotch tape and gel-assisted mechanical exfoliation techniques for preparation of 2D transition metal dichalcogenide flakes," *Micro Nano Lett.*, vol. 12, no. 12, pp. 970–973, Dec. 2017.

[104] G. Z. Magda, J. Pető, G. Dobrik, C. Hwang, L. P. Biró, and L. Tapasztó, "Exfoliation of large-area transition metal chalcogenide single layers," *Sci. Rep.*, vol. 5, no. 1, p. 14714, Oct. 2015.

[105] F. Pizzocchero *et al.*, "The hot pick-up technique for batch assembly of van der Waals heterostructures," *Nat. Commun.*, vol. 7, no. May, 2016.

[106] Y. H. Lee *et al.*, "Synthesis of large-area MoS_2 atomic layers with chemical vapor deposition," *Adv. Mater.*, vol. 24, no. 17, pp. 2320–2325, 2012.

[107] J. Jeon *et al.*, "Layer-controlled CVD growth of large-area two-

dimensional MoS2 films," *Nanoscale*, vol. 7, no. 5, pp. 1688–1695, 2015.

[108] Q. Ji *et al.*, "Epitaxial monolayer MoS_2 on mica with novel photoluminescence," *Nano Lett.*, vol. 13, no. 8, pp. 3870–3877, 2013.

[109] X. Ling *et al.*, "Role of the seeding promoter in MoS_2 growth by chemical vapor deposition," *Nano Lett.*, vol. 14, no. 2, pp. 464–472, 2014.

[110] L. Seravalli and M. Bosi, "A review on chemical vapour deposition of two-dimensional MoS_2 flakes," *Materials (Basel).*, vol. 14, no. 24, 2021.

[111] W. Chen *et al.*, "Oxygen-Assisted Chemical Vapor Deposition Growth of Large Single-Crystal and High-Quality Monolayer MoS_2," *J. Am. Chem. Soc.*, vol. 137, no. 50, pp. 15632–15635, Dec. 2015.

[112] H. Yu *et al.*, "Wafer-Scale Growth and Transfer of Highly-Oriented Monolayer MoS_2 Continuous Films," *ACS Nano*, vol. 11, no. 12, pp. 12001–12007, 2017.

[113] S. Li *et al.*, "Halide-assisted atmospheric pressure growth of large WSe_2 and WS_2 monolayer crystals," *Appl. Mater. Today*, vol. 1, no. 1, pp. 60–66, 2015.

[114] J. Zhou *et al.*, *A library of atomically thin metal chalcogenides*, vol. 556, no. 7701. 2018.

[115] S. Li *et al.*, "Vapour-liquid-solid growth of monolayer MoS_2 nanoribbons," *Nat. Mater.*, vol. 17, no. 6, pp. 535–542, 2018.

[116] S. Li *et al.*, "Wafer-scale and deterministic patterned growth of monolayer MoS_2 via vapor-liquid-solid method," *Nanoscale*, vol. 11, no. 34, pp. 16122–16129, 2019.

[117] J. Zhou. Jiadong, Lin. Junhao, Huang. Xiangwei, Zhou. Yao and Chen, Yu and Xia, Juan and Wang, Hong and Xie, Yu and Yu, Huimei and Lei, "A library of atomically thin metal chalcogenides," *Nature*, vol. 556, pp. 355–359, 2018.

[118] S. Li *et al.*, "Mixed-Salt Enhanced Chemical Vapor Deposition of Two-Dimensional Transition Metal Dichalcogenides," *Chem. Mater.*, vol. 33, no. 18, pp. 7301–7308, Sep. 2021.

[119] H. Liu *et al.*, "Growth of Large-Area Homogeneous Monolayer Transition-Metal Disulfides via a Molten Liquid Intermediate Process," *ACS Appl. Mater. Interfaces*, vol. 12, no. 11, pp. 13174–13181, Mar. 2020.

[120] S. Li, "Salt-assisted chemical vapor deposition of two-dimensional transition metal dichalcogenides," *iScience*, vol. 24, no. 11, p. 103229, 2021.

[121] M. Sharma, A. Singh, and R. Singh, "Monolayer MoS_2 Transferred on Arbitrary Substrates for Potential Use in Flexible Electronics," *ACS Appl. Nano Mater.*, vol. 3, no. 5, pp. 4445–4453, May 2020.

[122] H. Mantynen, N. Anttu, Z. Sun, and H. Lipsanen, "Single-photon sources with quantum dots in III-V nanowires," *Nanophotonics*, vol. 8, no. 5, pp. 747–769, 2019.

[123] H. Yang *et al.*, "Nanowire network–based multifunctional all-optical logic gates," *Sci. Adv.*, vol. 4, no. 7, 2018.

[124] F. Liang, H. Xu, X. Wu, C. Wang, C. Luo, and J. Zhang, "Raman spectroscopy characterization of two- dimensional materials," *Chinese Phys. B*, vol. 27, p. 037802, 2018.

[125] N. Kambhala, A. B. Kaveramma, S. Angappane, S. R. R, and S. Thiyagaraj, "Effects of the phase , morphology , band gap and hydrogen evolution of vanadium oxide with reduced graphene oxide," *Mater. Today Commun.*,

vol. 34, no. September 2022, p. 105478, 2023.

[126] S. Kellici, M. T. Sajjad, S. A. J. Thomson, and A. Rennie, "Outstanding visible light photocatalysis using nano-TiO_2 hybrids with nitrogen-doped carbon quantum dots and/or reduced graphene oxide," vol. 11, no. 18, 2023.

[127] W. Jie, Z. Yang, G. Bai, and J. Hao, "Luminescence in 2D Materials and van der Waals Heterostructures," vol. 1701296, pp. 1–35, 2018.

[128] R. W. Boyd, *Nonlinear Optics*, 3rd ed. New York: Academic Press, 2008.

[129] AnaPath, "ELECTRON MICROSCOPY," 2023. https://anapath.ch/electron-microscopy-2/

[130] A. Jacobs, "Photoelectron spectrometer, ESCALAB Mk II by Vacuum Generators," 2023. https://jacobs.physik.uni-saarland.de/home/index.php?page=steinbeiss/home_cms_steinbeissdet3-1&navi=service

[131] N. Ishida and V. S. J. Craig, "Direct Measurement of Interaction Forces between Surfaces in Liquids Using Atomic Force Microscopy," *KONA Powder Part. J.*, vol. 36, no. 36, pp. 187–200, Jan. 2019.

[132] S. B. Mitta *et al.*, "Electrical characterization of 2D materials-based field-effect transistors," *2D Mater.*, vol. 8, no. 1, p. 012002, Jan. 2021.

[133] C. Lee, H. Yan, L. E. Brus, T. F. Heinz, J. Hone, and S. Ryu, "Anomalous lattice vibrations of single- and few-layer MoS_2," *ACS Nano*, vol. 4, no. 5, pp. 2695–2700, May 2010.

[134] H. Li *et al.*, "From bulk to monolayer MoS_2: Evolution of Raman scattering," *Adv. Funct. Mater.*, vol. 22, no. 7, pp. 1385–1390, Apr. 2012.

[135] M. Gonzalez *et al.*, "Comprehensive analysis of the composition determination in epitaxial $Al_xGa_{1-x}As$ films: A multitechnique approach," *Mater. Sci. Semicond. Process.*, vol. 123, no. September 2020, p. 105469, 2021.

[136] Y. Li *et al.*, "Photoluminescence of monolayer MoS2 on $LaAlO_3$ and $SrTiO_3$ substrates," *Nanoscale*, vol. 6, no. 24, pp. 15248–15254, 2014.

[137] A. C. Ferrari and D. M. Basko, "Raman spectroscopy as a versatile tool for studying the properties of graphene," *Nat. Nanotechnol.*, vol. 8, no. 4, pp. 235–246, Apr. 2013.

[138] M. F. Khan *et al.*, "High performance complementary WS_2 devices with hybrid Gr/Ni contacts," *Nanoscale*, vol. 12, no. 41, pp. 21280–21290, Nov. 2020.

[139] M. Buscema, G. A. Steele, H. S. J. van der Zant, and A. Castellanos-Gomez, "The effect of the substrate on the Raman and photoluminescence emission of single-layer MoS2," *Nano Res.*, vol. 7, no. 4, pp. 561–571, Apr. 2014.

[140] A. Castellanos-Gomez *et al.*, "Local Strain Engineering in Atomically Thin MoS_2," *Nano Lett.*, vol. 13, no. 11, pp. 5361–5366, Nov. 2013.

[141] H. J. Conley, B. Wang, J. I. Ziegler, R. F. Haglund, S. T. Pantelides, and K. I. Bolotin, "Bandgap engineering of strained monolayer and bilayer MoS_2," *Nano Lett.*, vol. 13, no. 8, pp. 3626–3630, 2013.

[142] L. Du *et al.*, "Giant anisotropic photonics in the 1D van der Waals semiconductor fibrous red phosphorus," *Nat. Commun.*, vol. 12, no. 1, p. 4822, Dec. 2021.

[143] A. Henning *et al.*, "Charge Separation at Mixed-Dimensional Single and Multilayer MoS_2/Silicon Nanowire Heterojunctions," *ACS Appl. Mater.*

Interfaces, vol. 10, no. 19, pp. 16760–16767, 2018.

[144] D. S. Um, Y. Lee, S. Lim, S. Park, H. Lee, and H. Ko, "High-Performance MoS_2/CuO Nanosheet-on-One-Dimensional Heterojunction Photodetectors," *ACS Appl. Mater. Interfaces*, vol. 8, no. 49, pp. 33955–33962, Dec. 2016.

[145] Y. H. Lee *et al.*, "Fabrication of 1D Te/2D ReS_2 mixed-dimensional van der waals p-n heterojunction for high-performance phototransistor," *ACS Nano*, vol. 15, no. 2, pp. 3241–3250, Feb. 2021.

[146] M. H. Chiu *et al.*, "Determination of band alignment in the single-layer MoS_2 WSe2 heterojunction," *Nat. Commun.*, vol. 6, no. 1, p. 7666, Jul. 2015.

[147] X. Zhu *et al.*, "Effects of interlayer coupling on the excitons and electronic structures of WS_2/hBN/MoS_2 van der Waals heterostructures," *Nano Res.*, vol. 15, no. 3, pp. 2674–2681, 2022.

[148] S. Wang *et al.*, "Coherent coupling of WS_2 monolayers with metallic photonic nanostructures at room temperature," *Nano Lett.*, vol. 16, no. 7, pp. 4368–4374, 2016.

[149] D. E. Aspnes, S. M. Kelso, R. A. Logan, and R. Bhat, "Optical properties of Al_x $Ga_{1-x}As$," *J. Appl. Phys.*, vol. 60, no. 2, pp. 754–767, Jul. 1986.

[150] X. Duan, Y. Huang, Y. Cui, J. Wang, and C. M. Lieber, "Indium phosphide nanowires as building blocks for nanoscale electronic and optoelectronic devices," *Nature*, vol. 409, no. 6816, pp. 66–69, Jan. 2001.

[151] J. Wang, M. S. Gudiksen, X. Duan, Y. Cui, and C. M. Lieber, "Highly Polarized Photoluminescence and Photodetection from Single Indium Phosphide Nanowires," *Science (80-.).*, vol. 293, no. 5534, pp. 1455–1457, Aug. 2001.

[152] Q. Gao *et al.*, "Selective-area epitaxy of pure wurtzite InP nanowires: High quantum efficiency and room-temperature lasing," *Nano Lett.*, vol. 14, no. 9, pp. 5206–5211, Sep. 2014.

[153] X. Yuan *et al.*, "Carrier dynamics and recombination mechanisms in InP twinning superlattice nanowires," *Opt. Express*, vol. 28, no. 11, p. 16795, May 2020.

[154] O. Salehzadeh, M. Djavid, N. H. Tran, I. Shih, and Z. Mi, "Optically Pumped Two-Dimensional MoS_2 Lasers Operating at Room-Temperature," *Nano Lett.*, vol. 15, no. 8, pp. 5302–5306, Aug. 2015.

[155] J. Liu *et al.*, "Nonlinear optical absorption properties of InP nanowires and applications as a saturable absorber," *Photonics Res.*, vol. 8, no. 6, p. 1035, 2020.

[156] L. M. Malard, T. V Alencar, A. P. M. Barboza, K. F. Mak, and A. M. De Paula, "Observation of intense second harmonic generation from MoS_2 atomic crystals," *Phys. Rev. B - Condens. Matter Mater. Phys.*, vol. 87, no. 20, p. 201401, May 2013.

[157] A. Autere, H. Jussila, Y. Dai, Y. Wang, H. Lipsanen, and Z. Sun, "Nonlinear Optics with 2D Layered Materials," *Adv. Mater.*, vol. 30, no. 24, p. 1705963, Jun. 2018.

[158] J. Wallentin, D. Kriegner, J. Stangl, and M. T. Borgström, "Au-seeded growth of vertical and in-plane III-V nanowires on graphite substrates," *Nano Lett.*, vol. 14, no. 4, pp. 1707–1713, 2014.

[159] N. Bandaru *et al.*, "Effect of pressure and temperature on structural stability of MoS 2," *J. Phys. Chem. C*, vol. 118, no. 6, pp. 3230–3235, 2014.

[160] Z. Tian *et al.*, "Thermodynamics Controlled Sharp Transformation from InP to GaP Nanowires via Introducing Trace Amount of Gallium," *Nanoscale Res. Lett.*, vol. 16, no. 1, 2021.

[161] V. Senthilkumar, L. C. Tam, Y. S. Kim, Y. Sim, M. J. Seong, and J. I. Jang, "Direct vapor phase growth process and robust photoluminescence properties of large area MoS_2 layers," *Nano Res.*, vol. 7, no. 12, pp. 1759–1768, 2014.

[162] M. Mattila, T. Hakkarainen, H. Lipsanen, H. Jiang, and E. I. Kauppinen, "Enhanced luminescence from catalyst-free grown InP nanowires," *Appl. Phys. Lett.*, vol. 90, no. 3, pp. 1–4, Jan. 2007.

[163] P. Ren *et al.*, "Synthesis and optical properties of InP quantum dot/nanowire heterostructures," vol. 1902, no. 9, pp. 1898–1902, 2013.

[164] S. Cho *et al.*, "Phase patterning for ohmic homojunction contact in $MoTe_2$," *Science (80-.).*, vol. 349, no. 6248, pp. 625–628, Aug. 2015.

[165] Y. Tan *et al.*, "Controllable 2H-to-1T′ phase transition in few-layer $MoTe_2$," *Nanoscale*, vol. 10, no. 42, pp. 19964–19971, 2018.

[166] W. Zhang, Z. Huang, W. Zhang, and Y. Li, "Two-dimensional semiconductors with possible high room temperature mobility," *Nano Res.*, vol. 7, no. 12, pp. 1731–1737, Dec. 2014.

[167] H. Qiu *et al.*, "Hopping transport through defect-induced localized states in molybdenum disulphide," *Nat. Commun.*, vol. 4, no. 1, p. 2642, Oct. 2013.

[168] X. Liu *et al.*, "Charge Density Depinning in Defective $MoTe_2$ Transistor by Oxygen Intercalation," *Adv. Funct. Mater.*, vol. 30, no. 50, p. 2004880, Dec. 2020.

[169] S. J. Choi *et al.*, "Electrical and Thermoelectric Transport by Variable Range Hopping in Thin Black Phosphorus Devices," *Nano Lett.*, vol. 16, no. 7, pp. 3969–3975, Jul. 2016.

[170] S. Haldar, H. Vovusha, M. K. Yadav, O. Eriksson, and B. Sanyal, "Systematic study of structural, electronic, and optical properties of atomic-scale defects in the two-dimensional transition metal dichalcogenides MX2 (M=Mo, W; X =S, Se, Te)," *Phys. Rev. B*, vol. 92, no. 23, p. 235408, Dec. 2015.

[171] C. Rice *et al.*, "Raman-scattering measurements and first-principles calculations of strain-induced phonon shifts in monolayer MoS2," *Phys. Rev. B - Condens. Matter Mater. Phys.*, vol. 87, no. 8, p. 081307, Feb. 2013.

[172] N. Mao, Y. Chen, D. Liu, J. Zhang, and L. Xie, "Solvatochromic effect on the photoluminescence of MoS_2 monolayers," *Small*, vol. 9, no. 8, pp. 1312–1315, Apr. 2013.

[173] B. Chakraborty, A. Bera, D. V. S. Muthu, S. Bhowmick, U. V Waghmare, and A. K. Sood, "Symmetry-dependent phonon renormalization in monolayer MoS_2 transistor," vol. 161403, pp. 2–5, 2012.

[174] B. Radisavljevic and A. Kis, "Mobility engineering and a metal--insulator transition in monolayer MoS_2," *Nat. Mater.*, vol. 12, no. June, pp. 815–820, 2013.

[175] D. Ovchinnikov, A. Allain, Y.-S. Huang, D. Dumcenco, and A. Kis, "Electrical Transport Properties of Single-Layer WS_2," *ACS Nano*, vol. 8, no. 8, pp. 8174–8181, Aug. 2014.

[176] F. Ali *et al.*, "Metal–Insulator Transition Driven by Traps in 2D WSe_2 Field-Effect Transistor," *Adv. Electron. Mater.*, vol. 8, no. 9, p. 2200046,

Sep. 2022.

[177] S. Cho *et al.*, “Phase patterning for ohmic homojunction contact in $MoTe_2$,” *Science (80-.)*., vol. 349, no. 6248, pp. 625–628, Aug. 2015.

Aalto-DT 221/2023

ISBN 978-952-64-1589-5 (printed)
ISBN 978-952-64-1590-1 (pdf)
ISSN 1799-4934 (printed)
ISSN 1799-4942 (pdf)

Aalto University
School of Electrical Engineering
Department of Electronics and Nanoengineering
www.aalto.fi

BUSINESS +
ECONOMY

ART +
DESIGN +
ARCHITECTURE

SCIENCE +
TECHNOLOGY

CROSSOVER

DOCTORAL
THESES